Neutron background estimation for direct WIMP searches at SuperCDMS Soudan

Marina Peñalver Martínez

A Dissertation presented for the degree of
Master of Science in Particles, Strings and Cosmology

Supervised by:
David G. Cerdeño and Elías López Asamar

Institute for Particle Physics Phenomenology
Department of Physics
University of Durham

September 2016

Neutron background estimation for direct WIMP searches at SuperCDMS Soudan

Marina Peñalver Martínez

Submitted for the degree of
Master of Science in Particles, String and Cosmology September 2016

Abstract

Different pieces of evidence obtained during the last decade, from galactic to cosmological scales, has led to the conclusion that the Universe is dominated by a non-baryonic, non-luminous and non-relativistic matter contribution – commonly known as Dark Matter. Weakly Interacting Massive Particles (WIMPs) are one of the most popular candidates for the dark matter particle. In this work, a detailed description of the fundamentals of direct detection searches is offered, which aim to detect WIMPS via their interaction with a nucleus target in Earth-based detectors. The different backgrounds that will affect these experiments are described, together with the various techniques employed to reject them. SuperCDMS Soudan is a direct detection experiment which uses Germanium semiconductor crystals detectors operating at mK temperatures. These detectors are equipped with phonon and charge sensors, enabling excellent rejection of electron recoil backgrounds. However, any irreducible neutron background from environmental radioactivity is still present in the experiment. The estimation of this background is presented with a detailed description of the process followed, in the context of the search for WIMPs with masses between 10-100 GeV/c^2.

Acknowledgements

I would like to express my sincere gratitude to my supervisors David. G. Cerdeño and Elías López Asamar. Firstly, for accepting me to work with them in this project and giving me the opportunity to discover a field of physics which was completely new to me. And, above all, for their continuous support, advice, patience and motivation.

I would also like to thank my friends, who always offered me a helping hand and made this experience into something more than just a year of academic learning, showing me how lucky I am to have them in my life.

Lastly but not least importantly I would like to thank my family: my mum, aunt and grandma for making it possible for me possible to do this Master's and for providing me with unfailing support and continuous encouragement throughout my years of study – particularly throughout this year, where unfortunately I had to be away from them. It is also necessary to make a special mention about my grandfather, the one who – without being a scientist – instilled in me a love and curiosity for science when I was still a child.

Contents

Introduction

During the 1930's and 1970's, it was found that the internal dynamics of galaxy clusters and the rotations of galaxies could not be explained without the introduction of additional mass. This led to the idea of the existence of a mass component in the Universe that did not seem to emit or absorb electromagnetic radiation of any wavelength. This has since come to be known as Dark Matter (DM). Since then, that idea has been supported by various cosmological measurements, giving rise to model in which our Universe is not dominated by "normal" baryonic matter. Baryons only constitute a tiny fraction, $\sim 5\%$, of the energy content of the Universe, while DM supposedly contributes $\sim 25\%$, and dark energy $\sim 70\%$. These dark components played a crucial role in the evolution of the Universe, and the formation of the structures observed in the Universe at the present day.

It is believed that DM is composed of new particles which point to physics beyond the Standard Model (SM). Different candidates have been proposed, and this work focusses on the search for what is thought to be one of the most likely candidates, *weakly interactive massive particles* (WIMPs). Different experiments have been designed during the last few decades with the aim of finding explicit manifestations of the DM particles constituting the DM halo of the Milky Way. This work is mainly concerned with direct detection searches for WIMPs, which look for interactions of WIMPs with terrestrial targets. DM particles can also be detected indirectly via their annihilation products, or produced in particle colliders.

The expected low interaction rate of WIMPs with SM particles requires, in direct detection experiments, the introduction of sensitive detectors with low background rates. The SuperCDMS Soudan experiment is an upgrade of previous direct detection searches which used semiconductor crystal detectors operating at mK temperatures. To be able to comprehend the data collected by the experiment, it is necessary to obtain a thorough understanding of the background the experiment is exposed to. In the case of SuperCDMS, the final background which cannot be removed from the data is due to neutrons, generated from radioactivity in the surroundings of the laboratory and from the materials which compose the experiment. In this dissertation the estimation of such radiogenic neutron background is presented for SuperCDMS Soudan, based on the results obtained previously for the radioactivity contamination levels.

In Chapter 1, the principal pieces of evidence which led to the postulation of DM are presented, together with a discussion of the properties a DM candidate must fulfil and a summary of the principal candidates proposed during the last few decades. This chapter also contains a review of the different searches for DM either via direct detection, indirect detection or production in colliders, as well as their current status and future goals. Chapter 2 consists of a detailed description of the fundamentals on which direct detection experiments are based. The event rate of the WIMP-nucleus interaction is predicted and studied from the particle physics perspective via the presentation of different approaches to calculate the interaction cross section. From an astrophysical perspective,

the different velocity distribution profiles commonly considered for describing the velocity of the particles in the DM halo are introduced. Finally, the main background sources which can affect a direct detection search, their characteristic features, and techniques and cuts for background rejection are explained in detail.

The description of the SuperCDMS experiment is tackled in Chapter 3. This experiment is expected to yield an improvement on earlier DM searches. Semiconductor crystals operating at mK temperatures are used in SuperCDMS to search for a signal from DM particle interactions. Therefore, this chapter focuses on the detector technology, discussing details of the readout of the ionisation and phonon signal and the additional discriminating power of the detectors between electron and nuclear recoils, based on the ratio of these two signals. A detailed explanation is also offered about the different components of the shielding and their respective functions. SuperCDMS has been running since 2012 to summer 2014, and different results have emerged. The first and second CDMSlite test runs, low-mass WIMP search and a WIMP search between 10 and 100 GeV/c^2 are introduced. The last one is still in the data analysis phase, and the calculations presented in this dissertation are in the context of such analysis. An upgrade of SuperCDMS Soudan is currently under construction: SuperCDMS SNOLAB. It is expected to lead the direct detection searches for low-mass WIMPs, and the description of this experiment can be found in Section 3.5 .

Finally, in Chapter 4 the estimation of the radiogenic neutron background is presented for the WIMP search between 10 and 100 GeV/c^2. This chapter provides a detailed description of the estimation of the radiogenic neutron background, as well as the explanation of the process followed to calculate the radioactive contaminant levels.

Chapter 1

Evidence for dark matter, properties and detection

Although the existence of DM is solely inferred from its gravitational effects, it has become an accepted part of modern astrophysics. In this chapter, the principal evidence from galactic scales to cosmological scales are presented, and from them, the properties a DM particle candidate must fulfil are derived. Also, the most important candidates proposed during the last decades are introduced. Finally, a review of the different searches techniques employed for trying to detect DM, the main experiments which have taken place during the last decades and their current status are described.

1.1 Evidence for dark matter in the Universe

A wide array of evidence, from cosmological scales to galaxies, shows the presence of "missing matter" component which is not observed in the electromagnetic spectrum. In this section, a summary of the different pieces of evidence from different scales is presented.

1.1.1 Astrophysical evidence

The first hint of DM was provided by Zwicky in 1933, with his study of the dynamics of galaxy clusters. A few years later, Vera Rubin studied the rotational curve of spiral galaxies, and her results provided one of the clearest evidence of the existence of DM.

Galaxy clusters

Galaxy clusters are the largest gravitational bound systems in the Universe. In addition to a vast number of galaxies, they also contain a much bigger fraction of hot intracluster medium. The evidence of the presence of DM in galaxy clusters is provided by three different methods: cluster dynamics, X-ray emission from the intracluster medium and gravitational lensing.

Cluster dynamics. The first hints of DM were furnished by the study of clusters dynamic. In 1933, the Swiss-American astronomer Fritz Zwicky studied the redshifts of various galaxy clusters, which Edwin Hubble and Milton Humason published in 1931 [1]. He noticed a large scatter in the apparent velocities of eight galaxies within the Coma Cluster, with differences that exceeded 2000 km/s [2]. Firstly, Zwicky calculated the mass of the cluster via the product of the number of observed galaxies and using the average

mass of a galaxy estimated by Hubble. Posteriorly, estimating the distance and the size of the cluster, he applied the virial theorem, to calculate the total mass of the cluster via its potential energy.

$$2 < T >= - < V > \approx \frac{GM_{cluster}^2}{2 < r >}. \tag{1.1}$$

In 1937, Zwicky published a new article [3] with and extended analysis of the Coma Cluster. He obtained a mass-to-light ratio of around 500 for this cluster, leading him to the postulation of the presence of a relevant component of unseen matter in the cluster. This result was overestimated due to in this paper Zwicky used the last results at that moment to estimate the distances, which pointed to a Hubble constant of $H_0 = 558$ km/s/Mpc. Rescaling to the actual value of the constant of $H_0 = 67.27 \pm 0.66$ [4], the mass-to-light ratio obtained is 8.3. However, modern calculations of the mass-to-light ratio are similarly high, leading to the same conclusion: galaxy clusters are dominated by unseen matter.

X-ray emission of the intracluster medium. Most of the baryonic matter in clusters remains in the intracluster medium captured by the cluster's gravitational well. According to the virial theorem, as this gas falls into the centre of the gravitational well it is heated, emitting X-rays by thermal Bremsstrahlung. The emission spectrum is going to depend on the depth of the gravitational well. Thus, it does not only reveal the mass of the intracluster medium, but it can also help to map the DM distribution in the cluster.

Space telescopes, for instance, Chandra [5] and XMM-Newton [6], have elaborated maps of such X-ray emission, indicating cluster masses consistent with those obtained from cluster dynamics and gravitational lensing.

Gravitational lensing. One of the consequences of Einstein's General Theory of Relativity is that light rays are deflected by gravity [7]. Thus, one way of inferring the mass of a galaxy clusters is via the study of their effect upon light rays from distant sources. The image of distant known sources situated behind the object whose mass we are interested in calculating will be distorted into prominent arcs or rings, resulting in a multiple image source. Total mass estimated from gravitational lensing does not rely on the assumption of virial equilibrium.

The Bullet cluster. One of the most powerful confirmations about the presence of DM in galaxy clusters was recently observed. In 2006, a group of astronomers published an article [8] in which they observed a pair of merging clusters, commonly known as "Bullet cluster" (1E0657-558), Fig. 1.1. After the collision, the distribution of stars and galaxies was disconnected from the hot X-ray emitting gas, which comprises the majority of the baryonic mass in the cluster. A comparison of the weak lensing and X-ray maps clearly reveals that the mass in the cluster does not follow the distribution of baryons. An additional source of gravitational potential, as the one provided by DM, is necessary to explain that behaviour.

Galaxy dynamics

In the 1960s, Kent Ford developed an image tube spectrograph that Vera Rubin and himself used to perform spectroscopy observations of the Andromeda Galaxy. The observations of the M31 rotation curve that Rubin and Ford published in 1970 [9], show a discrepancy between the rotation curves predicted from photometry and those measured from 21 cm observations. From Newtonian mechanics, if the matter distribution of the

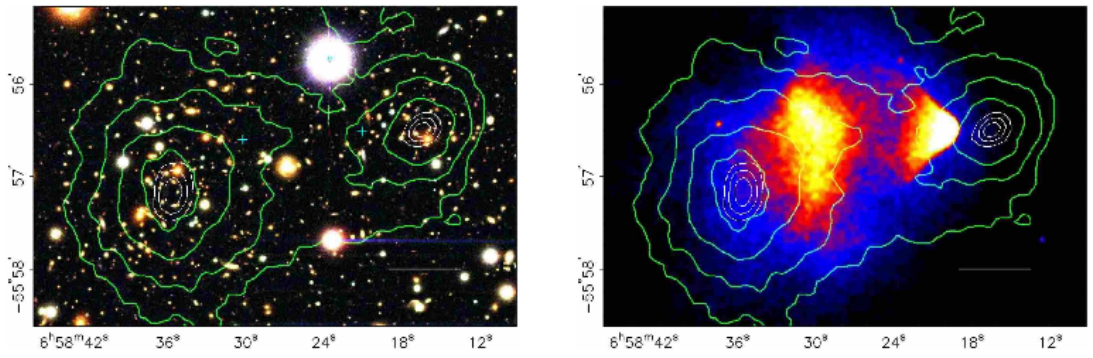

Figure 1.1: Bullet custer (1E0657-558) with weak gravitational lensing mass contours. Left: optical image from the Hubble Space telescope. Right: X-ray image from the Chandra X-ray Observatory [8].

galaxy would be described by the luminous matter we can observe, the orbital velocity of the galactic material outside the visible disk would decrease as $\sim r^{-1/2}$. However, the observed rotational curves are remarkably flat at high radii. If we consider a spherical mass distribution with total enclosed mass proportional to the radius, $M(r) \propto r$; the rotation curves predicted agree with the observations. Therefore, these measurements suggest that the visible matter is embedded in a substantially larger "DM halo", extended far beyond the visible disk.

1.1.2 Cosmological evidences

Modern cosmology is based on Einstein's General Theory of Relativity, and the assumption that the Universe is homogeneous and isotropic. The cosmological model commonly considered nowadays is called "Λ cold dark matter" (ΛCDM) cosmology. This model considers a universe with cosmological constant, Λ, and cold DM. In this model, $\Omega \simeq 1$ and at present day is dominated by the contributions of $\Omega_{0,M}$ and $\Omega_{0,\Lambda}$ [10, 11, 12]. The term "cold" indicates that most of the Universe's matter content was non-relativistic during the formation of large-scale structures. This is the simplest model which provides a proper explanation for the cosmic microwave background, the large-scale structure formation, the abundances of the light elements and the accelerating expansion of the Universe.

Cosmological observations and measurements reveal the presence of DM during the evolution of the Universe, and confirm the important role it played in the formation of the current structures in our Universe.

Nucleosynthesis in the early Universe The density of baryons can be determined by comparing the observations of the primordial abundances of light elements with the abundance predicted from Big Bang Nucleosynthesis [13]. Just after the Big Bang, during the next few seconds, the primordial abundances of deuterium ($^2_1$H), helium-3 ($^3_2$He), helium-4 ($^4_2$He) and lithium (Li) were formed from free protons and neutrons. Deuterium is not produced by any known astrophysical source, so its abundance is a particularly sensitive probe of the baryon density. Therefore, a lower bound on the primordial abundance can be obtained from any observed deuterium abundance. To explain the observed deuterium abundance a value of $\Omega_B h^2 \approx 0.02$ is needed [14]. This result means that baryonic matter constitutes just a small fraction of the total matter density in the Universe, leading to the

conclusion that the principal DM contribution must be non-baryonic.

Cosmic Microwave Background The cosmic microwave background (CMB) is the primordial black body radiation of the Universe, last scattered when the Universe was ∼300.000 years old [15]. The CMB is extremely well fitted by a black body spectrum at 2.73K, and the anisotropies found are at the 10 μK level. The fluctuations on the CMB temperature map inhomogeneities in the photon-baryon plasma at the era of decoupling. These inhomogeneities can be interpreted as incoherent acoustic waves in the plasma of the last-scattering surface. Therefore, position and amplitude of peaks in the power spectrum of CMB anisotropies are sensitive to both, the baryon and DM energy densities. The inertia of the oscillating plasma is increased by baryons, and reduced by DM upon the gravitational potential.

Using the last results obtained by Planck [4] observations of temperature and polarisation anisotropies of the CMB a value of $\Omega_b h^2 = 0.02226 \pm 0.00023$ for the baryonic matter density is acquired, which is consistent with the one predicted by BBN. The value obtained for the total matter density is: $\Omega h^2 = 01415 \pm 0.0019$, which reaffirms the idea that DM must be basically non-baryonic.

Large-Scale Structure Formation The most important problem regarding the structure formation in the Universe is trying to understand the evolution from the small perturbations in the very homogeneous early Universe to the actual large structures: galaxies, clusters, ... Since baryons and photons were tightly coupled at this era these fluctuations are a snapshot of the level of baryon inhomogeneity of the early Universe. The structures we see in the Universe today would have originated from this initial baryonic inhomogeneities. Regions with slightly higher density than their surrounding collapsed under their own gravity, giving rise to the seed of galaxy and clusters. These density fluctuations are represented as:

$$\delta(\bar{x}, t) \equiv \frac{\rho(\bar{x}, t) - \bar{\rho}(t)}{\bar{\rho}(t)}, \tag{1.2}$$

where $\bar{\rho}(t)$ is the mean energy density of the Universe at the time t.

To be able to reproduce the large structures observed at the present day, a value of $\delta \gtrsim 10^{-3}$ is demanded at the era of the last scattering, far greater than the one found in the CMB small scale anisotropies. N-body simulations show that the anisotropies observed in the CMB did not have enough time to grow to the structures seen in the Universe today. Non-baryonic DM solves this problem by decoupling the CMB from the total matter density of the Universe. The nearly smooth baryon distribution observed in the CMB small-scale anisotropies rapidly fall into the gravitational potentials of DM overdensities, which had more time to grow.

1.2 Properties and dark matter candidates

Although there is much unknown about the nature of DM, the evidence and observations already mentioned impose constraints in the features a DM particle candidate must fulfil.

1.2.1 Known dark matter properties

The first two properties a DM candidate must have can be deduced by the name used to refer to this unknown kind of matter. DM particles are *dark*; this relates to the fact that DM particles do not emit, absorb or scatter light. In addition, they travel through matter

unimpeded. Thus, DM particles do not interact by either the two strongest interactions: electromagnetism and strong nuclear interaction; remaining the question if they interact via the weak nuclear interaction. The second fundamental property is that DM particles interact gravitationally. Thus they must have *mass*. In fact, all the evidence we have of DM are derived from its gravitational effects. Besides this two basic properties more features of the DM particle candidates can be inferred from the observations mentioned in the previous section.

Neutral. Cosmological and astrophysical observations, together with laboratory tests, can establish constraints on heavy millicharged particles [16, 17, 18]. Upper bounds for the charge of the particles are then imposed. In the case of particles much heavier than the proton, the limit established for the charge of the particle is [17]:

$$\epsilon \leq 2.24 \cdot 10^{-4} \, (M/1TeV)^{1/2}. \tag{1.3}$$

Also, direct detection experiments put another upper bound in the charge of DM particles [19]:

$$\epsilon \leq 7.6 \cdot 10^{-4} \, (M/1\,TeV)^{1/2}. \tag{1.4}$$

Non-relativistic. Numerical simulations of the early Universe provide relevant information about the role DM played in structure formation. From these simulations is derived that DM particles must be cold, referring to the fact that DM particles were moving at non-relativistic speed at the beginning of structure formation. The distance a hot DM particle can travel before falling into a potential well is longer than for a cold DM particle. If DM were relativistic ,hot, at the epoch structure formation was beginning, the density fluctuations observed in the CMB would have shrunk rather than grew. In that case, the large-scale structure seen in the Universe could never have developed.

However, at galactic scale cold DM simulations lead to a larger number of DM haloes which would be observable through the luminous matter falling into their potential wells. This problem is solved if we consider warm DM, with a mass between 2-3 keV. Modern DM simulations also include baryonic matter, and they will be fundamental to determine if DM is warm or cold.

Non-baryonic. Combining the predictions from Big Bang nucleosynthesis and the data from the CMB only 4-5% of the total energy of the Universe comes from baryonic matter. Thus, DM particles must be predominantly non-baryonic.

Long-lived. Unless a conservation law prevents it, fundamental particles tend to decay into lighter particles. The footprints of DM are present in the CMB anisotropies, and its gravitational effects can be observed in galaxies and clusters of galaxies currently. Observations do not require DM particles to be stable, they could decay, but their lifetime must be longer than the age of the Universe. In this last case, DM particles would present very small couplings.

1.2.2 Dark matter candidates

A particle must fulfil the previous properties to be considered a possible DM candidate. Different candidates have been proposed since DM was postulated. However, the most commonly studied candidate is the *weakly interacting massive particle, WIMP*. It can arise in extensions of the SM such as supersymmetry or extra spatial dimensions, which

could either be flat [20] or warped [21]. Other massive candidates are 'SuperWIMPs' [22], 'SIMPZillas' [23] or 'Super-heavy relics' [24]. In this work only the principal candidates will be presented, including neutrinos, the natural SM candidate; and the pseudo-Nambu-Goldstone boson of the Peccei-Quinn solution to the strong CP problem, the axion.

Neutrinos

Neutrinos are the most natural candidate when one try to tackle the problem of finding a DM candidate from the SM perspective. Neutrinos are stable, or at least long-lived, and do not experience electromagnetic or strong interactions [25]. However, neutrinos were relativistic particles at the beginning of structure formation, so they can not account for the currently observed large-scale structure. On the other hand, the relic density today for neutrinos can be written as:

$$\Omega h^2 \approx \frac{\sum_i m_{\nu_i}}{91\, eV}. \tag{1.5}$$

The current bound for the masses of the three species of neutrinos is $\sum_i m_{\nu_i} \leq$0.3 eV. This leads to a value of $\Omega h^2 \leq 0.003$ which means that the contribution of neutrinos to the total DM density is less than 3%.

Sterile neutrinos Sterile neutrinos are similar to SM neutrinos. However, they do not experience SM weak interactions, apart from mixing. They were proposed as DM candidates in 1993 by Dodelson and Widrow [26]. Stringent cosmological and astrophysical constraints are imposed on sterile neutrinos derived from the analysis of their cosmological abundance and the study of their decay products. An explanation for the WMAP optical depth is reonisation of decaying particles, such as sterile neutrinos [27]. Also, they could be cold DM if a slight lepton asymmetry would exist, in which case they are produced resonantly with a non-thermal spectrum [28].

Axions

Axions arose as a solution to the strong-CP problem [29]. The Lagrangian of quantum chromodynamics includes a CP-violating term:

$$\mathbb{L} \supset \bar{\Theta} \frac{g^2}{32\pi^2} G^{a\mu\nu} G^{-}_{a\mu\nu}. \tag{1.6}$$

The Peccei-Quinn solution [30, 31] results in the postulation of a new particle: the axion [32, 33]. In this solution, $\bar{\Theta}$ is promoted from a parameter to a dynamical variable. Depending on the mass of the axion it can be considered a valid DM candidate. Different 'invisible' axion models, named so for their extremely weak couplings [29], are currently studied with masses in the range of $m_a \sim 10^{-6} - 10^{-4}$ eV. In an 'invisible' axion model, the Peccei-Quinn symmetry is decoupled from the electroweak scale and is spontaneously broken out a much higher temperature, decreasing the axion mass and its coupling strength. However, axions are not produced thermally. Thus, the axion DM hypothesis can not reproduce the correct DM abundance automatically.

Weakly Interacting Particles

For a particle species, to freeze-out of thermal equilibrium in the early Universe to become a cold relic, it must not be too light. Furthermore, for the predicted thermal relic abundance of such species to match the observed DM density, the DM particles must self-annihilate

with a cross section on the order of $\sigma v \sim 10^{-26}$ cm^3/s (where v is the relative velocity between the annihilating particles). This number is strikingly similar to the cross section that arises from the weak force. These conditions cover any number of stable particles with MeV-TeV masses and interactions that are mediated by the exchange of electroweak-scale particles. This observation, combined with theoretical arguments in favour of the existence of new physics at or around the electroweak scale, have elevated weakly interacting massive particles (WIMPs) [34] to the leading class of candidates for DM. Furthermore, WIMPs have motivated an expansive experimental program that continues to this day.

It is striking that a particle interacting with a typical weak scale cross section predicts a relic density close to the observed value $\Omega_{DM}h^2 \sim 0.1$. This fact is known as the "WIMP miracle".

Remarkably, solutions of the 'hierarchy problem' of the SM generally predict additional particles with weak scale masses $\sim$100 GeV/c^2 and additional symmetries to stabilise the particle on cosmological timescales.

Supersymmetry (SUSY) [35] provides a series of candidates for WIMP DM. It is a natural extension of the SM which requires that for every fermion, a boson must exist with the same quantum number and vice versa. This extension leads to a whole new family of possible particles, and some of the superpartners of known particles have been considered as potential DM candidates.

Neutralino. Neutralinos are probably the most studied and most popular SUSY DM candidate [36, 37], and a concrete example for a WIMP. The lightest neutralino χ_1^0 appears in the minimal supersymmetric standard model (MSSM) [38] as the lightest mass eigenstate among the four neutralinos. A detailed description of the features of this candidate can be found in [39].

Sneutrinos. Sneutrinos are the extension for SM neutrinos in SUSY. If their mass is in the range of 550-2300 GeV/c^2, a cosmologically interesting relic density is obtained [40]. However, their existence was ruled out due to the scattering cross section of a sneutrino with nucleons is much larger than the limits found by DM detection experiments.

Gravitinos. Gravitinos are the superpartner of graviton in supersymmetric models. Gravitinos only interact gravitationally, being really hard to observe [41]. In some supersymmetric scenarios, gravitinos can be the lightest SUSY particle and be stable [39].

Axinos. Axinos are the superpartner of axions in supersymmetric models. They were considered only to be able of acting as warm or hot DM candidates. However, recently it has been demonstrated that for low enough reheating temperature, cold axino DM may be possible [41].

1.3 Detection of dark matter

Many experiments are currently working with the aim of detecting DM particles. If WIMPs exist, they could be detected via the identification of their annihilation products, by their interaction with atomic nuclei on earth detectors or by production at particle colliders. These three search categories are complementary since they give different information about the details of DM-SM particles interactions, Fig. 1.2. Thus, before extracting any

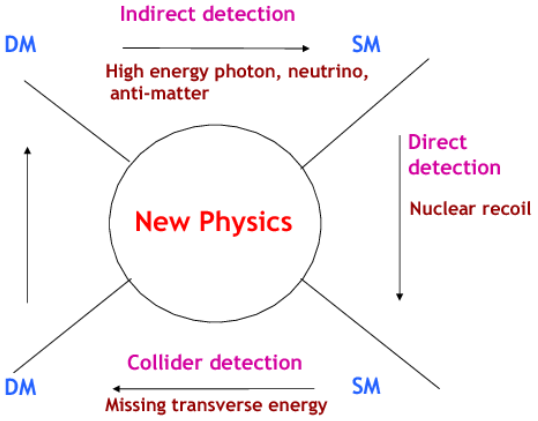

Figure 1.2: Diagram relating the different DM searches techniques.

conclusion is necessary to compare the results obtained by the combination of the three types of searches.

This section consists of a description of the techniques employed by the different type of searches and a summary of the current status of the experiments involved in them. It will restrict to WIMP searches, considering that WIMPs are one of the most theoretical supported DM candidates and the majority of the experiments which currently are taking place are focused on this purpose.

1.3.1 Indirect detection of dark matter

Indirect searches aim to detect the products originated by annihilations or decays of DM particles in the shape of fluxes of charged particles, photons or neutrinos. The key point of these searches is to look for excesses of these particles which can not be explained by ordinary astrophysical processes. It is necessary to look for channels and ranges of energy where the background can be removed. For instance, in the case of charged particles the search is focused on antiparticles, less abundant in the Universe; and, in the case of neutrinos and photons, in areas where the DM abundance is expected to be large.

Considering WIMPs as the most likely DM candidate, these DM particles are expected to annihilate in pairs into the SM particles. More precisely, in order to reproduce the correct relic abundance a velocity annihilation cross section of value $\langle\sigma\rangle = 3 \cdot 10^{-26}\, cm^3/s$ is expected [42]. These annihilation processes would be the ones generating the cosmic rays that indirect detection experiments are searching for. Another possibility is that they could be produced by the decay of DM particles, provided that their half-life is long enough that such process decay does not deplete the cosmological density significantly.

The results given by the most important indirect detection searches are shown in Fig. 1.3, at the end of this section.

Indirect detection via charged cosmic-rays

Electron and positrons. As mentioned above, the particles which constitute the DM halo of the Milky Way are expected to annihilate or decay into pairs of SM particles in different channels, such as: $b\,\bar{b}$, $\mu^+\mu^-$, $\tau^+\tau^-$ ... These primary particles after decaying, and due to the processes of showering and hadronizing, give origin to fluxes of energetic cosmic-rays: e^-, e^+, $\bar{p}$, ...

The signal obtained for cosmic-rays proceeding from DM sources would have some distinctive features that might help to distinguish them from the ones generated by an ordinary astrophysical source. In general, all of the spectra will present a 'bump'-like shape, characterized by a high-energy cutoff at the DM particle mass. These bumps and rises will be situated in the range of TeV and sub-TeV, and in particular, for $e^{\pm}$ they will also present a softly decreasing tail at lower energies [42].

The e^-, e^+ and $\bar{p}$ produced in the halo propagate immersed in the turbulent galactic magnetic field. The field while propagating produces scattering of charged particles so that their journey can be described as a diffusion process from an extended source, the DM halo. Unlike the ordinary cosmic-rays, mainly originated in the disk.

Therefore, these annihilations or decays will follow the DM density distribution in the galactic halo. The different models proposed to describe such distribution differ even by several orders of magnitude at the galactic centre, but are roughly normalised at the same value at the location of the Earth [43]. For that reason, the observables depending mostly on the local DM density will not be very affected by the choice of the profile, being those sensitive to the density at the galactic centre will be affected the most.

Since 2008, a series of positive results have been announced by indirect detection experiments pointing in excesses of e^- and e^+ at the TeV and sub-TeV scale. These results are striking because they imply the existence of a source of primary e^- and e^+ other than the known ones. Nevertheless, it does not mean that the new source could be itself of unknown astrophysical nature. Future experiments are expected to solve this question and be able to discriminate between a DM origin and an astrophysical one. AMS-02 collaboration will measure precisely the positron fraction spectrum at high energies [44], expecting its behaviour to solve the question.

A quite more promising approach consists of identifying the arrival direction of the cosmic leptons. Detecting a clear dipole anisotropy would mean a clear indication of the existence of a single point source while measuring an isotropic distribution would rather favour a diffuse source such as DM. [42]

Antiprotons. In the antiproton channel, data have been published by PAMELA satellite since 2008 till 2012 [45] and more recently AMS-02 has also presented preliminary data on the $\bar{p}/p$ ratio. The data-sets obtained in both experiments are in good agreement. However, unlike in the leptonic case, the results does not reflect and unambiguous excess in antiproton fluxes. On the other hand, data shows a preference for a flat proportion in $\bar{p}/p$, which is hard to explain by current astrophysical models. This may point to propagation schemes, characterised by a relatively mild energy dependence of the diffusion coefficient at high energies. [42]. The fact that no clear excess was found makes possible to derive constraints, as shown in Fig. 1.3.

Antideuterium. Antideuterons are considered as a quite promising tool for DM searches. They can be produced by DM via the coalescence of an antiproton and an antineutron originating from an annihilation event [46]. The flux of $\bar{d}$ from DM is supposed to be much lower than for the rest of possible annihilation products. Nevertheless, what makes detection via $\bar{d}$ promising is that the flux expected peaks in an energy region, typically a fraction of a GeV, where very little astrophysical $\bar{d}$'s background is present.

Currently, only one upper limit exists, it comes from the BESS experiment, and it is about two order of magnitude higher than the most optimistic predictions [47]. The GAPS experiment will use a balloon mission to slow down the $\bar{d}$ nucleus, capture them inside the

detector forming an exotic atom to obtain a characteristic X-ray and pion radiation due to the annihilation [48].

Indirect detection via gamma-rays

DM annihilation processes can produce photons in different ways. One type will be prompt γ-rays produced directly by DM annihilation themselves, following the DM halo distribution closely. Also, secondary radiation is expected, emitted by the $e^{\pm}$ produced by the annihilation process. In this case, the spatial distribution varies depending on the process originating the radiation, see section 3 of [42].

The election of the best targets plays a major role in these experiments. The principal targets at which the experiments look are: The Milky Way Galactic Centre, the Galactic Centre Halo, broad regions of the Galactic Halo such as observational windows centred at galactic centre, globular clusters, subhalos of the galactic DM halo, satellite galaxies of the Milky Way, large-scale structures in the relatively nearby Universe and the Universe at large, meaning looking at the isotropic flux of γ-rays that come to us from DM annihilation in all halos and all along the recent history of the Universe [42].

The current main experiments are the FERMI satellite and the ground-based Imaging Atmospheric Čerenkov Telescopes (IACT) HESS, MAGIC and VERITAS. Any of them could find clear results so bounds on the annihilation cross section are imposed. In the future an important role is expected to be played by Čerenkov Telescope Array (CTA) [49], High Altitude Water Čerenkov Observatory (HAWC) [50] and the Large High Altitude Shower Observatory (LHAASO) [51].

The Galactic Center GeV excess. Since 2009, several authors have reported the detection of a γ-ray signal in FERMI data, coming from the inner few degrees around the galactic centre [52]. The study of the spectrum and morphology showed that the data is compatible with the one expected from the annihilation of DM particles. Precisely, the best fits are obtained with particles of masses in the range of 30-50 GeV/c^2 distributed following the NFW profile and annihilating into $b\bar{b}$ with $\langle\sigma_v\rangle = (1.4 \pm 2)10^{-26}\,\mathrm{cm}^3/\mathrm{s}$ [53]. The presence of this excess is evident and it has been observed that it is robust against variations of the known astrophysical foregrounds. However, it could also be produced by some unknown astrophysical phenomena in that region: point sources, leptonic or other outbursts, non-conventional cosmic-ray propagation or injections of cosmic-rays [42].

An open question is the possibility of confirming the DM source interpretation by association with other signals, for instance, in antiprotons or γ-rays from dwarfs.

Indirect detection via neutrinos

Neutrinos are also expected to be part of the products in DM annihilation. Since they barely interact with matter, proceed straight and substantially unabsorbed through the Galaxy, they go across vast distances. Detection is made using massive Čerenkov detectors located underground, under-ice or under-water. They are detecting via the showers of secondary particles that they produce when interacting, either in the experiment or the surroundings. Čerenkov detectors allow measuring the energy and direction of the particles. With the aim of distinguishing the background, mainly cosmic muons originating from the atmosphere, the experiment only select upgoing tracks, i.e. produced by neutrinos that have crossed the entire Earth.

The main neutrino telescopes, such as SUPERKAMIOKANDE, IceCube [54] and ANTARES [55], have looked for signals without finding any.

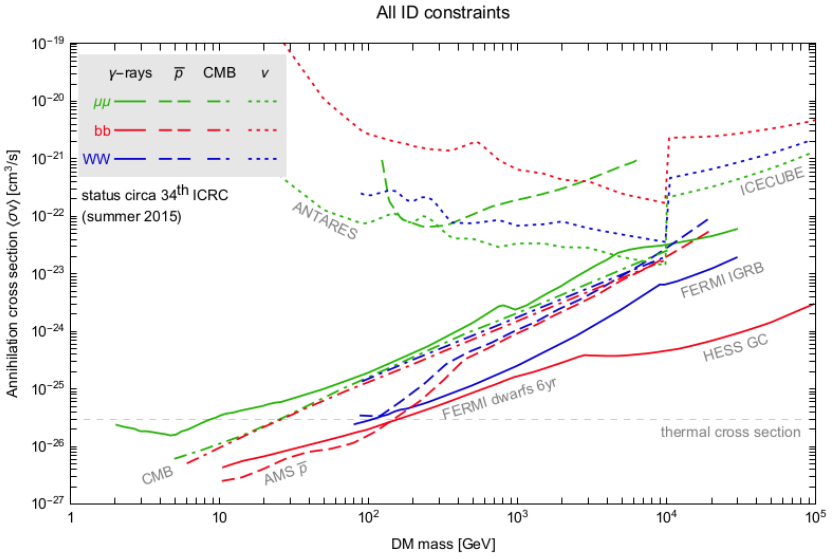

Figure 1.3: Current bounds in DM annihilation cross section for WIMPs in different channels and different indirect detection experiments.[42]

1.3.2 Direct detection of dark matter

DM direct detection searches aim to detect, in ultra-clean and ultra-sensitive experiments, the recoil of an atom hit by a DM particle. The first direct detection experiments took place at the 1980s, but it was in the late 1990s when the advanced searches started with the first experiments to achieve event-by-event active discrimination against backgrounds [56]. Direct detection experiments require the construction of deep underground detectors to detect the possible interaction of DM particles with SM particles directly. The energy spectra for a 100 GeV/c^2 WIMP interacting with different targets are shown in Fig. 1.4.

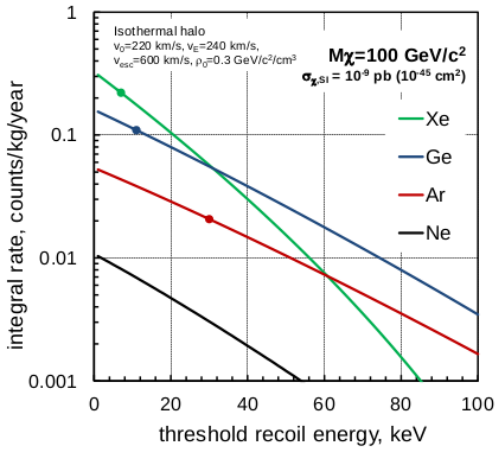

Figure 1.4: Predicted integral spectra for WIMP elastic scattering for Xe, Ge, Ar and Ne, assuming perfect energy resolution. The rates are calculated for a WIMP of mass 100 GeV/c^2 and 10^{-45} cm^2 interaction cross section per nucleon.[56]

Direct detection experiments generally do not measure the nuclear recoil (NR) energy

directly. The total energy deposited by a particle interaction with the target is reconstructed from the experimental measurements, for instance, NR or electron recoil (ER). Conversion between the two energies must be calibrated for each experiment depending on the target and experimental technique. Regularly γ sources are used to calibrate ERs, and neutron sources are employed to calibrate NRs.

One of the main advances in recent direct detection searches is the use of detectors capable of establishing a discrimination between electron and NRs, reducing the background significantly. Various technologies achieve this discrimination: differentiating ionisation versus phonon energy deposition for electron and NRs (CDMS); ionisation versus scintillation, using two-phase noble liquid; fast versus slow scintillation, using liquid Argon and liquid Neon; and scintillation versus phonons (CRESST).

With the aim of reducing the background these direct searches are exposed to, the experiments must be located in deep underground laboratories, reducing significantly the cosmic-ray interactions capable of producing neutrons. Decay products of radioactivity originated in the environment and the materials of the experiments are another strong source of background. This radioactive background makes necessary the shielding of the detectors to protect them from neutrons result of fission or (α,n) reactions. The signal produced by a scattering from a neutron is a NR that could be indistinguishable from that produced by a WIMP.

In this section, a summary of the different techniques employed, the main direct detection experiments and future experiments that will use them. Also, the results provided by the different experiments and the predictions for the future ones are shown in Fig. 1.5.

Cryogenic Solid State

Cryogenic solid state detectors include ionisation radiation spectrometers and bolometric detectors using dual-signal readout techniques [56].

The first published limits for direct detection searches were done using high-purity Germanium (Ge) detectors operating near liquid nitrogen temperature ($\sim$90 K). This technique is employed by experiments as CoGeNT, TEXONO and MALBEK presenting excellent energy resolution, low energy thresholds and commercial target availability. These detectors only measures ionisation, ERs from γ and β radiation are thus indistinguishable from the NRs neutrons or WIMPs can produce.

However, cryogenic solid detectors operated at temperatures $<$100 mK can distinguish ERs from NRs on an event-by-event discrimination, leaving radiogenic neutrons as the main potential background. These detectors were pioneered by the CDMS collaboration, operating with Ge and Silicon (Si) detectors, firstly at Stanford University and later at the Soudan Underground Laboratory. The technology was further developed by European groups with Germanium (EDELWEISS) and calcium tungstate (CRESST). For SuperCMDS and EDELWEISS collaborations the two signal readout techniques are phonons, heat, and ionisation, and phonons and scintillation light for CRESST. SuperCDMS iZIP and EDELWEISS-II Ge detectors suppress surface β decays strongly by interleaving ionisation and phonon sensors.

The sensitivity to low-mass WIMP achieved by these detectors is comparable to that obtained with high-purity Ge experiments. CRESST also reaches similar low-mass performance with $CaWO_4$ crystals.

Currently, the results from SuperCDMS Soudan are waiting to be analysed, and a new experiment, SuperCDMS SNOLAB, is being developed. EDELWEISS and CRESST have proposed EURECA, a new experiment which will employ Ge detectors.

Liquid Xenon

Liquid Xenon (LXe) presents important advantages as target for WIMP. It can be highly purified, is chemically inert, and is radiopure [56]. γ background is easily removed in these experiments, due to the high density and atomic number γ-rays have a short interaction length. A large enough LXe detector acts as its own shielding, obtaining an inner fiducial volume (FV), see section 2.2, with a very low background rate. The fact that neutrons tend to produce multiple-scattering in the dense liquid is used to reduce neutron background.

The current implementation of XMASS employs more than 830 kg of LXe [57]. The application of an electric field drifts the ionised electrons in LxE to the surface of the liquid where they can be extracted. Also, dual-phase time projection chambers allow determining the position of the interaction in three dimensions.

The experiment XENONT1 is currently at the commissioning phase at the Laboratori Nazionali del Gran Sasso in Italy with a sensitivity of $1.6 \cdot 10^{-47}$ cm^2 and with 1 tone of FV [58]. Another relevant experiment using this technique is LUX (Large Underground Xenon), it consist of a dual-phase Xenon time-projection chamber with 250 kg of active liquid mass. In October 2013, the LUX collaboration reported results from 85.3 live-day exposure of a 118 kg fiducial mass [59].

Liquid Argon

The design employed in Liquid Argon (LAr) experiments is basically the same than for Liquid Xenon. Single-phase LAr detectors rely upon the collection of the scintillation light in the hard UV, induced in Argon by energy depositions. This energy deposited is proportional to the total amount of scintillation light recorded, and it is the timing structure of the scintillation pulse the one which depends on the nature of the event [56]. These experiments reach an excellent pulse shape discrimination if the energy deposition is significant enough. However, the relatively large energy threshold limits sensitivity to WIMPs with very low masses. Argon experiments have the problem of the presence of an intrinsic radioactive background from ^{39}Ar, natural isotope in atmospheric Argon. To solve this problem, the use of Argon recovered from underground sources was proposed [60].

These detectors are typically spherical chambers, allowing the most efficient light collection, although due to their cost larger detectors may be cylindrical. Dual-phase Argon detectors are very similar in design to the LXe detectors, with an electric field used to extract the ionisation released in the interaction.

Examples of single-phase experiments are MiniCLEAN [61] and DEAP-3600 [62], both placed at SNOLAB. In the case of dual-phase detectors, it stands out the collaboration DarkSide, with the experiment DarkSide-50 located in Gran Sasso laboratory and which published the first results in 2014 [63].

Superheated Liquid Detectors

Threshold detectors experiments combine bubble chambers and superheated droplet detectors. The term weakly superheated is referred to the local energy deposition from a NR will generate bubble nucleation. β and γ events will not produce bubbles, and acoustic signals are employed to reduce α events. To obtain an energy spectrum, due to the lack of an energy measurement on a per event basis it is necessary to perform threshold scans by varying the operational temperature and pressure.

SIMPLE experiment operated in its first version with 0.2 kg active volume of superheated C_2ClF_5 droplets and achieved a threshold of 8 keV [64]. The experiment published a spin-dependent limit at a WIMP mass of 35 GeV/c^2 of $5.3 \cdot 10^{-39}$ cm^2 and a spin-independent limit of $4.8 \cdot 10^{-42}$ cm^2. After this first experiment, the collaboration carried out a second version, SIMPLE Phase II [65].

Other two experiments are PICASSO and COUPP [66]. These two collaborations decided to merge their efforts with a single ton-scale experiment, known as PICO [67] and placed at SNOLAB underground laboratory.

Scintillating Crystal Detectors

Another technique employed in direct detection experiments is scintillating inorganic crystals, such as NaI and CsI. The main advantages of these crystals are their high efficiency as scintillators, the low target costs and the well understood technologies for light collection and detection over broad areas. Scintillation pulse shape discrimination reached levels of electromagnetic background rejection of 90-99% in the deployed experiments. Coincidences between elements of multi-crystal arrays and the annual modulation expected for the WIMP signal are also employed as rejection background techniques.

The DAMA/LIBRA [68, 69] has been operating since 2003 a DM search with a setup of 250 kg of NaI. They observed an annual modulation in the data obtained in the experiment at greater than 9σ significance, with a phase consistent with the expected from galactic DM interactions. However, this signal is in strong tension with results of many other experiments which ruled out that area of the phase-space in which this supposed signal would situate DM positive detection.

Many experiments attempt to reproduce the DAMA/LIBRA experiment in order to check the same signal region to test if the annual modulation is confirmed. The ANAiS collaboration is running an experiment at the Canfrac Underground Laboratory, and the full experiment would have used 112.5 kg of ultrapure NaI[70]. The KIMS experiment ran until December 2012 [71] and reported limits inconsistent with the DAMA/LIBRA modulation detection. Another experiments are PICO-LON [72] and DM-Ice, placed in the IceCube array at the South Pole [73].

Directional Detectors

The movement of the earth in the Milky Way produces a 'WIMP wind' coming from constellation Cygnus [74]. The other backgrounds a direct direction experiment is exposed to, except neutrinos, are expected to be isotropic. Then detectors capable of differentiating the direction of the NR will offer a huge discrimination background power.

With this purpose, low-pressure gas time projection chambers are employed, providing the 3D track reconstruction. The big two challenges these experiments need to face are deploying enough gas target mass to be sensitive to the supposed low rate of WIMP interactions and reaching the technique necessary to obtain a low energy threshold.

This technique was first developed in the DRIFT collaboration using negative ion drifting in CS_2 and CF_4 at the Boulby mine [75]. Other important experiments which employ this kind of detectors are NEWAGE [76] and MIMAC [77].

Current situation

Direct detection experiments explore regions of theory parameter space, some of which are completely inaccessible via collider or indirect detection experiments. Every direct

detection search reports a new limit in the parameter space, restricting the region where WIMPs are expected to be detected and contributing with essential information about the nature of DM particles. A summary of the limits reported by direct detection experiments and the sensitivities expected to reach for future experiments are shown in Fig. 1.5.

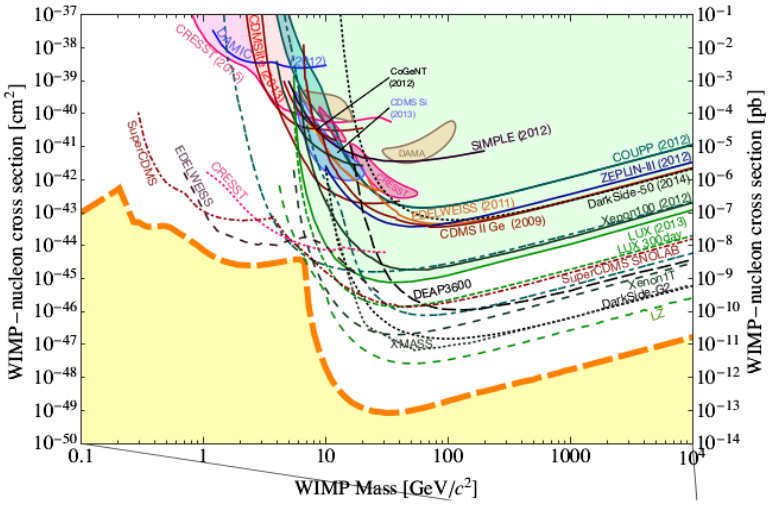

Figure 1.5: Current bounds in $m_\chi - \sigma_{WN}$ in Direct Detection searches and their projected sensivity.[42]

1.3.3 Dark matter production in colliders

Accelerator searches aim to create DM particles in the laboratory from collisions of SM particles. Due to the small interaction cross section and long life, DM, if produced in a collision, will escape to the detector without depositing any energy or momentum. Therefore, the signature of any DM particle at a collider will involve missing transverse energy and momentum [78]. In this summary, we will present experiments where the DM particle is explicit; and, in particular, collider searches at the Large Hadron Collider (LHC) [79].

The main drawbacks accelerator searches present are the impossibility of proving stability of the DM candidate beyond the apparatus or distinguishing single from multiple new invisible particles; a poor mass resolution on the invisible, and they may have no handle on the nature of the interaction, particle type, quantum number, ... [80].

Production of DM at colliders can be classified into two categories. In the first one, new heavy states are first produced, decaying through a cascade down to the lighter stable DM particles. For example, Supersymmetry with R-parity conservation and on-shell production of a Higgs boson. The second production mode is the one in which DM particle is produced directly. For instance, the pair creation of DM particles through some off-shell mediator.

Non-LHC accelerator searches are focusing mainly on a portal to an assumed dark sector through a new dark vector boson, which couples to the SM through kinetic mixing with the regular photon [81]. Due to the weak coupling, and potentially low mediator mass, the allowed parameter space goes beyond the reach of the LHC, and high-intensity searches or future B-meson factories, at fixed-target experiments provide and alternative option.

Dark matter production models at the LHC

There are three different approaches when modelling DM production at the LHC [80].

Full models, where DM is considered as a part of a UV-complete theory, allow for coherent modelling of all interactions, decay channels, ... SUSY in the for of the MSSM [38] is a clear example of this kind of approach. Due to the huge parameter space which arises in these models it is often necessary to make assumptions to reduce the complexity.

A second modelling approach is effective field theories (EFT). In this case, the particle mediating between the SM and the DM is integrated out, so the interaction can be described approximatively as an effective four-point interaction. The main advantage is that it consists of a model-independent approach, and the parameter space is just restricted to the mass of the DM particle and the EFT scale $\Lambda = M_* = M/\sqrt{g_\chi g_q}$, where M is the mass of the mediator, and g_q and g_χ are the couplings of the mediator to the quarks and the DM, respectively. In this context the comparison with results obtained in direct detection searches is straightforward. However, EFTs present some limitations. To be a realistic model, the mass of the mediator should be much larger than the energy in each collision. The energy scales at the LHC shrink the range of applicability to masses of the mediator in the TeV range or higher. Another limitation is that in this approach, usually a single operator is assumed to describe the interaction, which is not necessarily the case. Finally, in some corners of the phase space, unitarity and perturbativity should be explicitly checked.

In between full models and the EFT approach simplified models appear. In this models, the new physics is restricted to only what is relevant to describe a certain experimental final-state topology under consideration. Simplified models extend the SM with a few particles, explicitly specifying the mediator and interactions with the DM particle. Even if simplified models are not realistic full models, they are an excellent tool or interpreting the results of the LHC SUSY searches in the LHC runs at 7 and 8 TeV proton-proton centre of mass collisions [82, 83]. For the ongoing 13 TeV run, also the searches for direct production of DM are making the transition to simplified models as their principal instrument for interpretation of the results [84, 85, 86].

ATLAS [87] and CMS [88] detectors at the LHC used the full LHC Run-1 dataset of about $\sim$20 fb^{-1} of proton-proton collisions at 8 TeV centre of mass energy.

The searches in the monojet, mono-W/Z and monophoton final states will be presented below. All of them have as main feature a central particle radiated from a quark line in the initial state of the hard collision, providing the recoil necessary to make the pair of produced DM particles emerge in the detector as missing transverse momentum, E_T^{miss}.

In the monojet searches [89, 90], the event selection commences with the E_T^{miss} trigger used, fully efficient for events with E_T^{miss} typically about 200 GeV. Electron, muon and tau vetoes are used to reject the large leptonically-decaying W background; leaving $Z \rightarrow \nu\nu$ as the dominant remaining background, with $W \rightarrow l\nu$ contribution subdominant. The estimation of these two dominant background components is done using $Z \rightarrow l^+l^-$ and $W \rightarrow l^\pm\nu$ control event samples, accounting for the leptons as undetected particles to mimic the DM.

Also, the case where a W or Z boson is produced recoiling off the DM, and decaying hadronically to two quarks was also considered [91, 92]; as well as its leptonic counterpart where DM particle recoils against a single lepton or a pair of leptons [93, 94]. The main two backgrounds these searches are exposed to are: W and ZZ production. Both of theme are accurately predicted using simulation.

Several other searches have been performed by ATLAS and CMS collaborations. Such as monophoton searches [95, 96], in which a single photon from QED initial state radiation

recoils against E_T^{miss} from DM.

LHC results must be compared to the limits obtained by direct and indirect detection experiments in order to achieve robust conclusions. It is significant to emphasise the importance of the collider searches for low-mass DM particles. Indeed, where at low mass the energy deposits in direct detection experiments is below the threshold energy, and therefore is too low for efficient detection, the collider setting yields a maximised missing momentum, and thus sensitivity, at zero mass. In addition, another way different searches complement each other is related to the fact that direct detection experiments exhibit typically little sensitivity to spin-dependent interactions, allowing the collider searches to have complementary coverage also at intermediate masses. At higher mass, the collider searches see the cross sections being kinematically suppressed; here indirect searches probe complementary ground.

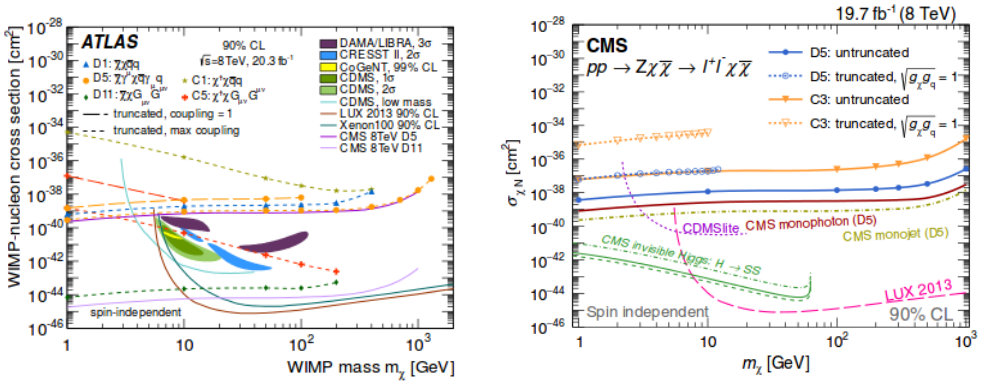

(a) (b)

Figure 1.6: Results from ATLAS and CMS collaborations.

The graphics which present the actual searches of indirect detection experiments and the respective one for direct detection experiment and production in colliders must be compared to extract the maximum information about the current state of DM searches. Comparing these graphics with the different particle models proposed the exclusion limits offer a visual information about which candidates are being excluded and what experiments will explore regions related to a particular candidate.

Chapter 2

Direct detection of dark matter

Direct detection experiments aim to detect WIMPs via their elastic scattering off atomic nuclei. Due to the Milky Way's DM halo, in the case it is composed by WIMPs, the Earth is exposed to a flux on the order of $10^5(100\ \mathrm{GeV/m_\chi})\ \mathrm{cm^{-2}\ s^{-1}}$ [97]. Even though WIMPs are weakly interacting, this flux is large enough to expect a measurable fraction of WIMPs producing elastic scattering in low background detectors [98]. The rate of these interactions will depend on astrophysical properties of the Milky Way DM's halo and the particle model considered for WIMP interactions. A theoretical and general calculation of the expected WIMP-nucleus event rate for detectors in Earth can be derived. The dependence on the model considered to describe the WIMP-nucleus coupling is taken into account in the differential cross section.

Each direct detection experiment aims to measure the rate, R, and the spectrum of the recoil energy, E_R, of the NRs. This purpose requires identifying candidate events among a far larger background rate.

2.1 Predicted WIMP event rate in direct detection searches

WIMP-nucleus relative speed is of order 100 $\mathrm{km^{-1}s^{-1}}$. Therefore the interaction will take place in the non-relativistic limit. Simplifying the calculation of the recoil energy of the nucleus, which takes the form:

$$E_R = \frac{\mu_N^2 v^2\,(1 - cos\theta^*)}{m_N}, \tag{2.1}$$

where μ_N is the WIMP-nucleus reduced mass, m_N is the mass of the nucleus, v is the DM particle velocity in the detector frame, and θ^* is the scattering angle in the centre of mass frame.

To obtain the number of detected DM particles, N, is necessary to multiply the DM flux by the effective area of the target. This calculation will be carried here as follows. First, as a simplification, monochromatic DM particles moving all with the same velocity are considered; and second, the convolution of this result with the velocity distribution is discussed.

The DM flux in the monochromatic case is defined as $\phi = n\,v$, where n is the DM number density. The effective area of the target is given by the product of the total number of targets, N_T, and the scattering cross section, σ_{WN}. Finally, the resulting value has to be multiplied by the live time, L, that is defined as the total amount of time in which detectors are ready to detect a new signal.

$$N = n\,v\,N_T\,\sigma_{WN}\,L. \tag{2.2}$$

By this equation, the differential event number is obtained, which shows the dependence on the energy of the number of detected DM particles. It is also necessary to consider that not all of the WIMPs in the halo have the same velocity, but it is described by a local velocity distribution function $f(v)$. The different profiles usually considered to describe this velocity distribution will be explained in Section 2.1.2. Thus, we have to integrate over all possible velocities.

$$\frac{dN}{dE_R} = L\, n\, N_T \int\limits_{v_{min}} \frac{d\sigma_{WN}}{dE_R}\, v f(v)\, dv \tag{2.3}$$

Considering that $n = \rho_0/m_\chi$ and $N_T = M_T/m_N$, where ρ_0 is the local density of WIMPs and M_T is the total mass of the detector. For a WIMP of mass m_χ and a nucleus with mass m_N the differential even rate is given by:

$$\frac{dR}{dE_R} = \frac{\rho_0}{m_N m_\chi} \int\limits_{v_{min}} \frac{d\sigma_{WN}}{dE_R}(v, E_R)\, v f(v)\, dv, \tag{2.4}$$

where we have divided Eq. 2.3 by the experimental exposure, $\epsilon = L\, M_T$.

The event rate is the quantity measured in a direct detection experiment, and it is commonly expressed in terms of counts/kg/day/keV. The lower limit of integration, denoted as v_{min}, is given by the minimum WIMP speed which can cause a recoil of energy E_R, and is equal to: $v_{min} = \sqrt{(m_N E_R)\,/\,\left(2\mu_N^2\right)}$. The upper limit is the local escape velocity of WIMPs in the Milky Way.

The total event rate is found by integrating the differential event rate over all possible recoil energies in a given experimental window:

$$R = \int\limits_{E_T} dE_R\, \frac{\rho_0}{m_N m_\chi} \int\limits_{v_{min}} \frac{d\sigma_{WN}}{dE_R}(v, E_R)\, v f(v)\, dv, \tag{2.5}$$

where E_T is the threshold energy, the smallest recoil energy which the detector is capable of measuring. This threshold energy limits the exploration of low-mass WIMPs.

The event rate and total number of events detected in the experiment are related, as mentioned before, by the experimental exposure in the following way:

$$N = \epsilon \cdot R \tag{2.6}$$

Note that Eq. 2.5 receives two different contribution. The first one comes from particle physics due to the explicit presence of the cross section in the equation. The second one is the astrophysics contribution coming from the presence of the velocity distribution. In the next section, the particle physics input is explained, and in the following section, the astrophysics input is introduced.

2.1.1 WIMP-nucleus interaction cross section

The WIMP-nucleus event rate on earth detectors presents an explicit dependence on the interaction cross section. The WIMP-nucleus differential cross section depends on the particle model we are considering for the microscopic description of WIMPs, and it will depend fundamentally on the WIMP-quark interaction strength. Standard WIMP scattering calculations make simplifying assumptions about the type of interaction between

the nucleon and the DM particle. In general, the WIMP-nucleus differential cross section is separated into a spin-independent and a spin-dependent contribution:

$$\frac{d\sigma_{WN}}{dE_R} = \left(\frac{d\sigma_{WN}}{dE_R}\right)_{SI} + \left(\frac{d\sigma_{WN}}{dE_R}\right)_{SD}. \tag{2.7}$$

These contributions must be added coherently, using nuclear wave functions [97].

When the nucleus is light the DM particle perceives it as a point-like particle, with no substructure. However for heavy nuclei is necessary to consider the form factor, $F(E_R)$, which accounts for the spatial extent of the scatter. It encodes the dependence on the momentum transfer that in the non-relativistic limit takes the form:

$$q = \sqrt{2\, m_N E_R}. \tag{2.8}$$

This form factor leads to a suppression of the event rate for heavy WIMPs of nucleons [99]. We then can express the differential cross section as:

$$\frac{d\sigma_{WN}}{dE_R} = \frac{m_N}{2\mu_N^2 v^2}\left(\sigma_0^{SI} F_{SI}^2(E_R) + \sigma_0^{SD} F_{SD}^2(E_R)\right). \tag{2.9}$$

The σ_0 are the cross sections at zero momentum transfer.

Recently, an effective field theory approach for WIMP scattering has been developed that uses a more complete set of operators that can appear in the effective Lagrangian that describes the WIMP-nucleus interaction. These operators rely on a range of nuclear properties, added to the standard spin-independent and spin-dependent contributions. It also explicitly includes isospin interference and interference between operators, giving rise to a space of possible DM interactions that are very sensitive to the specific choice of detector material [100],[101],[102].

The contributions to the cross section arise from different terms in the microscopic Lagrangian. For example, the spin-independent cross section can receive contributions from scalar and vector couplings to quarks, while the spin-dependent part of the cross section can have its origin in axial-vector couplings. These contributions are characteristic of the specific WIMP candidate and can be potentially useful for their discrimination in direct detection experiments.

Spin-independent contribution

Spin-independent contributions to the WIMP-nucleus interaction cross section come from scalar-scalar and vector-vector couplings in the Lagrangian, L:

$$L \supset \alpha_q^S \bar{\chi}\chi\bar{q}q + \alpha_q^V \bar{\chi}\gamma_\mu\chi\bar{q}\gamma^\mu q, \tag{2.10}$$

where α_q is the coupling of the WIMP field, χ, to the quark field, q. The contribution from the scalar coupling leads to the following expression for the WIMP-nucleon cross section,

$$\sigma_0^{SI,S} = \frac{4\mu_N^2}{\pi}\left(Z f^p + (A-Z) f^n\right)^2, \tag{2.11}$$

for a nucleus with mass number A and atomic number Z; and with coupling constants to proton and neutrons f^p and f^n, respectively.

The vector coupling, present for a Dirac fermion but which vanishes for Majorana particles, gives rise to an extra contribution. Only valence quarks contribute to the vector current leading to the following expression:

$$\sigma_0^{SI,V} = \frac{\mu_N^2 B_N^2}{\pi}, \tag{2.12}$$

with

$$B_N \equiv \alpha_u^V (A+Z) + \alpha_d^V (2A-Z). \tag{2.13}$$

For a general WIMP with scalar and vector interactions, the spin-independent contribution to the scattering cross section would read:

$$\left(\frac{d\sigma_{WN}}{dE_R}\right)_{SI} = \frac{2m_N}{\pi v^2}\left[[Zf^p + (A-Z)f^n]^2 + \frac{B_N^2}{4}\right] F^2(E_R). \tag{2.14}$$

In most cases, the WIMP coupling to neutrons and protons is very similar, $f^p \approx f^n$, and therefore the scalar contribution can be approximated by

$$\left(\frac{d\sigma_{WN}}{dE_R}\right)_{SI}^{S} = \frac{2m_N A^2 (f^p)^2}{\pi v^2} F^2(E_R). \tag{2.15}$$

The spin-independent contribution basically scales with the square of the mass number, A. It gives an idea of the dependence of the interaction on the mass of the nucleus.

Spin-dependent contribution

The spin-dependent contributions to the WIMP-nucleus scattering cross section are produced by the coupling of the DM particle field to the quark axial current $\bar{q}\gamma_\mu\gamma_5 q$. For instance, in case the WIMP is a fermion, the Lagrangian would contain the following term:

$$L \supset \alpha_q (\bar{\chi}\gamma^\mu\gamma_5\chi)\left(\bar{q}\gamma_\mu\gamma^5 q\right) \tag{2.16}$$

Axial-vector couplings generate amplitudes proportional to WIMP and nucleus spin. The coupling to the spin of protons and neutrons is characterised by the coefficients a_p and a_n. In the limit of zero momentum transfer, the spin-dependent interaction cross section is:

$$\sigma_0^{SD} = \frac{32\,\mu_N^2 G_F^2}{\pi}\left(\frac{J+1}{J}\right)(a_p\langle S_p\rangle + a_n\langle S_n\rangle)^2, \tag{2.17}$$

where J is the nucleus spin and $\langle S_{p,n}\rangle$ is the expectation value for the nucleus proton or neutron spin. The spin-dependent interaction amplitude with two nucleons of opposite spin interferes destructively in the zero-momentum transfer limit. Since nucleons pair by opposite spin in the nucleus, the interaction rate is dominated by unpaired nucleons.

The couplings a_p and a_n depend in sign and magnitude on the DM particle model we are considering. The resulting differential cross section then can be expressed as:

$$\left(\frac{d\sigma_{WN}}{dE_R}\right)_{SD} = \frac{16\,m_N}{\pi v^2}\frac{(J+1)}{J}G_F^2(a_p\langle s_p\rangle + a_n\langle S_n\rangle)^2 \tag{2.18}$$

The spin-dependent contribution is proportional to $\frac{J+1}{J}$ while spin-independent one scales as the square of the mass number, A. Although in general both have to be taken into account, most of the experiments are more sensitive to one of the two contributions.

The scalar component dominates for heavy targets ($A > 20$), and most of the experiments which are taken place are based on targets with heavy nuclei such as Silicon ($A \sim 28$), Germanium ($A \sim 73$), or Xenon ($A \sim 131$); making them more sensitive to the spin-independent contribution. Nevertheless, experiments exist that are also sensitive to the spin-dependent WIMP coupling through the choice of targets with a large nuclear angular momentum, for instance, ^{19}F. Also, an important role in spin-dependent searches is played by Xenon detectors. Xenon isotopes, ^{129}Xe and ^{131}Xe, have unpaired nucleons so Xenon detectors are sensitive to spin-dependant interactions.

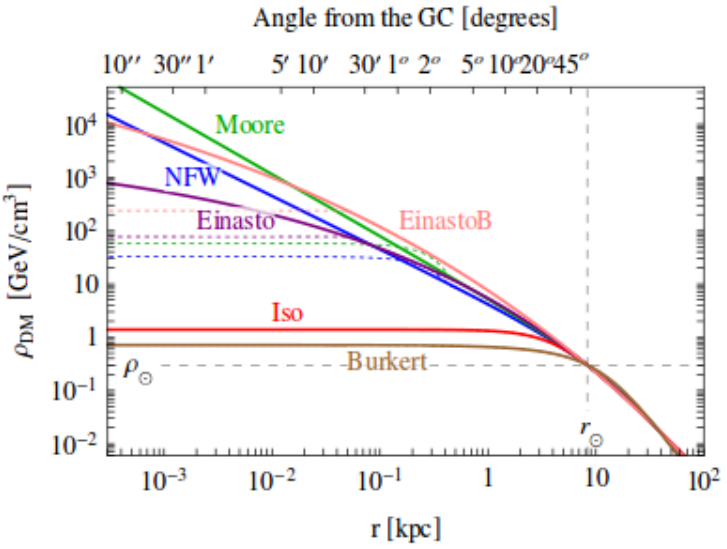

Figure 2.1: DM profiles for different halo models.[105]

2.1.2 Dark matter density distribution in the Milky Way halo

The WIMP-nucleus differential event rate is energy dependent mainly because of the kinematics of elastic scattering, combined with the dynamics and speed distribution of WIMPs. In addition, the movement of the Earth with respect to the Galactic rest frame induces a time and directional dependence in the recoil rate [97]. The combination of these features gives a characteristic shape to the WIMP signal, which is crucial for the identification of WIMPs in direct detection experiments.

In addition to the already mentioned dependence on the particle model (implicit in the differential cross section), the event rate also depends on the local WIMP density, ρ_0, and on the velocity distribution $f(v)$ of the DM particles in the Milky Way halo. Different profiles are considered to describe the local distribution; they apply observational constraints to astrophysical models of the Milky Way.

The simplest one is the so-called Standard Halo Model. It assumes DM is distributed spherically, isotropically and smoothly with density profile $\rho \propto r^{-2}$. The velocity distribution in the galactic rest frame for such a model follows a Maxwell-Boltzmann distribution:

$$f(\vec{v}) = \frac{e^{-\frac{|v|^2}{2\sigma^2}}}{\sqrt{2\pi\sigma}}, \tag{2.19}$$

where the one-dimensional velocity dispersion, σ, is related to the circular speed, v_c, as $\sigma = \sqrt{3/2}\, v_c$. The canonical value is $v_c = 220$ km s^{-1}, with a statical error of order 10% [103]. Using the solar radius $R_0 = (8.0 \pm 0.5)$ kpc, it gives a value for the local dark matter density of around $\rho_0 = 0.3$ GeV/cm^3. This value is commonly considered in direct detection experiments but, depending on the profile, it can vary from $(0.2 - 0.6)$ GeV/cm^3 [104]. The Standard Halo Model is commonly used in calculations of exclusion limits.

Although Standard Halo Model profile is widely used, as a first simplification, the accuracy is improved by numerical simulations. These simulations contained, traditionally, only DM and showed triaxial velocity distributions. The resulting halos feature, however, cusped profiles with steeper density variations towards the centre of the halo, while observations favoured flatter cored profiles [104]. Based on the result of these refined numerical

simulations or direct observations [106, 107] different models are considered both in indirect detection and indirect detection. These models differ by several orders of magnitude at the galactic centre but they present roughly agreement in the value of the local density. The most commonly used density profiles are Navarro-Frenk-White (NFW) and the Einasto, both of them present a cusp at the galactic centre; the truncated isothermal or the Burkert one, with a central core [105], as shown in Fig. 2.1.

Due to these differences between the different profiles in every direct detection experiment is necessary to specify which particle model we are considering and also the density profile we are using.

2.2 Backgrounds

Possible WIMP masses cover a huge range from 1 GeV to 100 TeV and expected interaction cross sections with SM particles vary from 10^{-40} to 10^{-50} cm^2 [56]. WIMPs would interact with nucleons by elastic scattering with nuclei, requiring detection of NR energies in the 1-100 keV range. This is the scale of nuclear processes, which will become the backgrounds these searches are exposed to. Therefore direct detection experiments have to be capable of identifying WIMPs events among a far larger background rate.

2.2.1 Main background sources

As mentioned before, the interaction with the detectors expected by WIMPs is on order of $\sim$1 event per year. On the other hand, the flux from environmental radioactivity and cosmic muons is on the order of $\sim$1 event/cm^2 min each. Therefore given the extremely low frequency of the expected signal and the typical scale of the recoil energy, the environmental background would overburden the signal if not controlled.

Hard work is done designing experiments with the aim of reducing as much as possible these background signals from the collision between known particles and target nuclei. Therefore, the ultimate sensitivity of a direct detection experiment is determined by the rate of background events which are indistinguishable from WIMP candidates. The main strategies to reject background are via shielding, use of pure materials and reduction in data analysis.

The backgrounds to be considered are the ones produced by environmental radioactivity and cosmic muons. The environmental contribution to the background comes from isotopes as ^{232}Th, ^{238}U and ^{40}K embedded in solids, as well as from the materials surrounding the experiment and in the materials which compose the experiment itself. Also, another source of environmental radioactivity to be considered is the one produced by the decay of ^{222}Rn to ^{238}U. This isotope is in gas state, therefore it can leave the rocks being part of the air and penetrating in the experiment.

The products of this environmental radioactivity are mainly: α, β and γ radiation and neutrons, plus some heavy nuclei. Unlike WIMPs, these particles can be blocked thanks to a physical shielding. However, any shielding is never going to be able to achieve a total background rejection and, also, it will only protect from the external radiation.

Charged particles

^{238}U and ^{232}Th chains produce a series of α and β decays, as shown in Fig. 2.2. They are present in the rock surrounding the laboratory and also in the materials which compose the setup of the experiment. Detectors themselves, are expected to be highly radiopure and their contribution is considered negligible. Unlike WIMPs, these charged particles

present a short free path, on the order of ∼1 mm. Penetration range of radiation has an exponential dependence on the distance, so substantial part of the events produced by α and β particles will take place in the region close to the surface of the detectors. Surface events can suffer from reduced ionization collection, see Section 3.1, so backgrounds events for WIMPs via ERs are not properly discriminated. If the detectors of the experiment are sensitive to the position of the interaction a cut to remove this background can be applied. This cut selects events in the innermost part of the detector, called fiducial volume (FV). Therefore, the detector itself acts as self-shielding and the interactions close to the surface are mostly rejected.

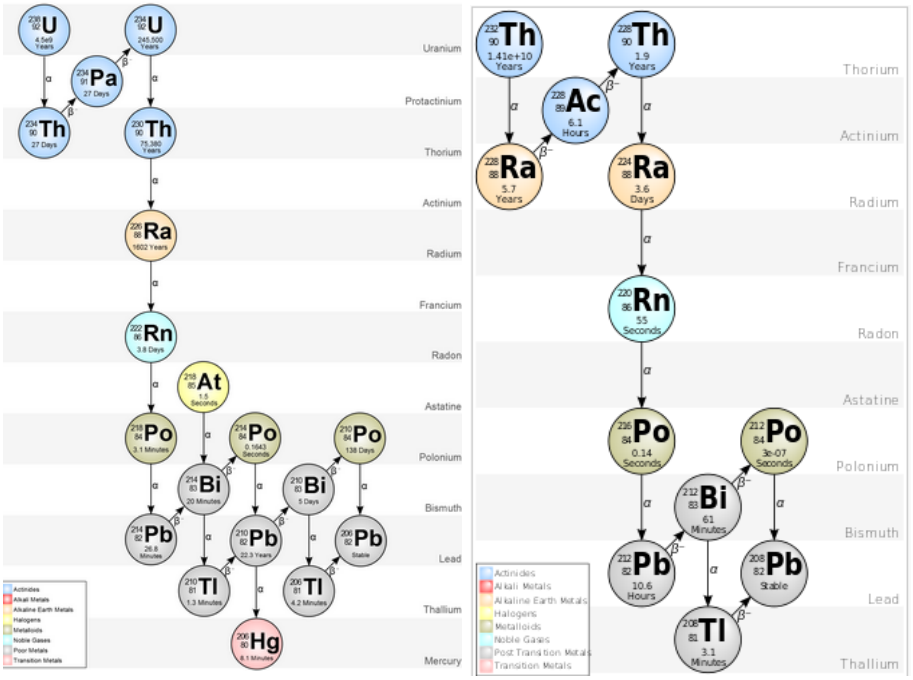

(a) (b)

Figure 2.2: (a). ^{238}U decay chain. (b). ^{232}Th decay chain.

Gamma-ray radiation

γ-rays are mainly emitted from chain decays of ^{238}U and ^{232}Th, as well as from common isotopes as ^{40}K, ^{60}Co or ^{137}Cs present in the surrounding materials.

^{238}U and ^{232}Th chains produce a series of α and β decays, as already mentioned, accompanied by the emission of several γ-rays with energies from tens of keV up to 2.6 MeV [104]. γ-rays interact with matter via photoelectric effect, Compton scattering and e^- e^+ pair production [108]. An electron is produced in all of these interactions depositing its energy as an ER in the region of interest for DM searches, few keV. Thus, γ-rays produce ERs when they interact with the target. The particles collide with the electrons which act, in some sense, as a shielding for the true WIMP target: the nucleus.The possibility of a WIMP-electron collision is not null, but its cross section is expected to be much smaller.

In experiments whose detectors are prepared for exploiting the differences between electron and nuclear recoils, the reduction of these backgrounds becomes easier. However, if the detectors of the experiment are not arranged for this discrimination, γ-ray could affect the sensitivity of the experiment in the WIMP signal region.

γ-rays from natural radioactivity outside the experimental setup can be reduced shielding the detector with a high atomic number and high-density material; lead is commonly used for that purpose. Then, γ-rays produced inside the different volumes of the experimental setup become in the main γ source. To reduce their contribution, only high-purity materials are used in the construction of the experiment.

Finally, the remaining background can be rejected using different cuts, taking into account the differences between gamma interaction and expected WIMP interaction. Multiple simultaneous hits are removed due to the negligible probability of DM particles to interact more than once in the experiment. The mean free path of γ-rays is on order or $\sim$1 cm. Therefore, FV cut will not be as effective with γs as it is rejecting α and β particles.

Radiogenic and cosmogenic neutron background

Neutrons with energies on the order of few MeV can produce signals in the range of keV, the region of interest for WIMP detection. Besides, neutrons produce NRs making their single-scatterings indistinguishable from WIMPs. Thus, they become in an irreducible background for DM searches. This background can not be discriminated using event properties, and therefore the rejection of neutrons must be achieved with the shielding and the use of high-purity materials. In addition, data analysis require an estimation of the neutron background expected in order to compare with the observed number of events.

The contribution to the neutron background can be divided into cosmogenic and radiogenic neutrons. Cosmogenic neutrons can be generated through spallation, muon-induced nuclear disintegration, or various secondary processes within muon-induced hadronic and electromagnetic showers. These neutrons have energies up to several GeV and are moderated by the surrounding materials to energies of few MeV. In addition, radiogenic neutrons are emitted in (α,n) and spontaneous fission reactions from natural radioactivity, either in the surrounding materials or in the ones employed in the experiment itself. Radiogenic neutrons have lower energies, few MeV [104].

In order to minimise the number of cosmogenic neutrons, DM direct detection experiments are placed in underground laboratories. The deeper the location, the lower the muon flux. In Fig. 2.3 the reduction of the muon flux due to the depth of the laboratory is shown for different underground laboratories. The flux of radiogenic neutron background produce inside the experiment can be reduced by choosing high-purity materials. For instance, low in uranium and thorium, whose decay chains are commonly the main source of this type of neutrons. Detector shielding is used to reduce the external neutron flux, moderating them to energies below the threshold energy. Neutrons interact with the nucleus, so the materials with the highest moderating power will be the ones with a light nucleus, as they will receive more energy. Due to their contents of hydrogen and their relatively high density usually polyethylene (C_2H_4) and water are used. In addition, active shielding is designed to record interactions of muons, making really easy to discard muon-induced neutron interactions. Muon vetoes can be improved through water Cherenkov detectors which present higher muon tagging; they are also efficient stopping neutrons.

Finally, to reduce further the neutron background data analysis techniques are applied. As mentioned in the previous section, multiple-scattering interactions are removed. A FV cut and yield discrimination are not effective for neutrons as they interact homogeneously in all the detector volume and they produce NRs.

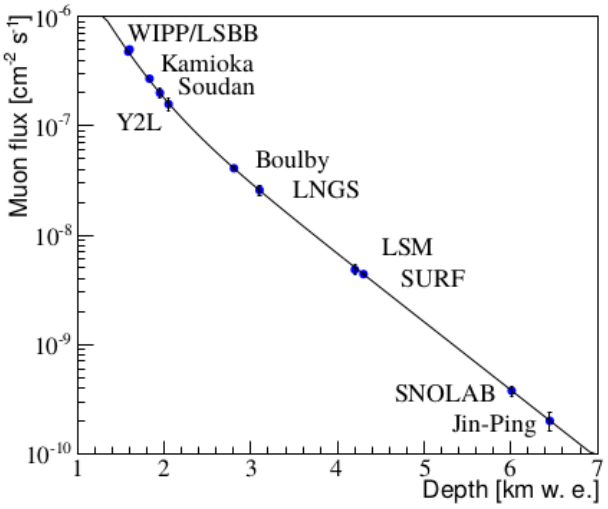

Figure 2.3: Muon flux as a function of depth in km water equivalent for various underground laboratories hosting DM experiments.[104]

Neutrino background

The background from neutrinos is not currently affecting DM searches. However, it will need to be considered in future experiments. A study about how neutrino signal could affect a potential WIMP detection can be found in [109].

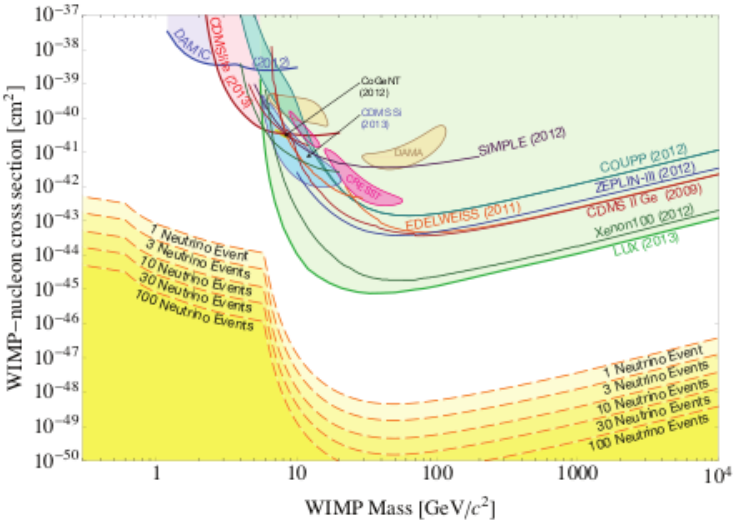

Figure 2.4: Neutrino isoevent contour lines compared with exclusion limits.[109]

Neutrinos can produce either neutrino-electron and neutrino-nucleus elastic scattering. The latter interaction has not been measured yet so it could be detected for the first time in DM searches during the next few years. Direct detection experiments will be sensitive to the flux of solar, atmospheric and diffuse supernova neutrinos. ^{8}B solar neutrinos are

supposed to produce an energy spectrum and event rate equivalent to a WIMP of 6 GeV/c^2 , with a spin-independent cross section on the nucleon of $\sim 5 \cdot 10^{-45}$ cm^2. Whereas the atmospheric neutrino background would induce an energy spectrum and event rate that is similar to the one generated by a $\sim$ 100 GeV/c^2 WIMP with a spin-independent cross section of $\sim 10^{-48}$ cm^2. [110]. In principle, in the case of a possible positive signal, the modulation of the signal along the year could be considered to distinguish WIMPs from neutrinos. Also, directional detection experiments will be useful as one of the main neutrino sources will be the Sun, making possible with this strategy to reduce significantly solar neutrinos background.

Direct detection experiments are improving their sensitivity via more sophisticated detectors and an increase in their masses. Upcoming DM direct detection searches with target masses over one tonne and sensitivity to keV energies will start being sensitive to neutrinos from astrophysical sources. It can be seen in Fig. 1.5, comparing with 2.4, that exclusion limits of experiments are getting closer to this neutrino background.

Chapter 3

The SuperCDMS experiment

SuperCDMS is an update to the CDMS (Cryogenic Dark Matter Search) and CDMS II experiments, and has been running as a five-tower installation of Ge detectors in the Soudan Underground Laboratory in Minnesota, located in an iron mine 714 m underground. The rock overburden provides 2090 meters water equivalent (mwe) of shielding against cosmic radiation; this reduces the surface muon flux by a factor of $\sim 5 \cdot 10^4$. In addition to the natural shielding provided by the chosen location, SuperCDMS employs both passive and active shielding with the aim of reducing the external photon and neutron backgrounds from radioactive and cosmogenic sources.

The experiment aims to detect directly NRs from the elastic scattering of WIMP on the nuclei of semiconducting crystals cryogenically cooled to ~ 50 mK. The target consists of fifteen 0.6 kg cylindrical Ge crystals distributed in groups of three to form the five towers. The high-purity semiconductor crystal is held at that low temperature using a ^{3}He-^{4}He dilution refrigerator.

The current experiment in Soudan operated between March 2012 and December 2015 and is in the process of analysing data with an analysis optimised for WIMPs with masses above 10 GeV/c^2. A new generation of experiments will be based at SNOLAB and is expected to have excellent sensitivity to low-mass WIMPs (<10 GeV/c^2).

3.1 Semiconductor technology

SuperCDMS employs high-purity Ge crystals as detectors. Therefore, it is of high importance to understand the physics behind these crystals to be able to extract the correct information about the interaction of the different particles with them. When a particle interacts in the detectors it produces ionization and phonons. After a collision with an energetic particle, the recoil energy of the target is deposited into the crystal in two parts: 1) valence electrons are excited into the conduction band producing electron-hole charge carrier pairs (*ionisation*), and 2) high-frequency lattice vibrations in the crystal are produced (*phonons*). Upon absorption into electrodes at the detector surface, the de-exciting charge carriers release their excitation energy in a third form of lattice vibration: *recombination phonons*. Therefore, in this case, the total phonon energy is equal to the recoil energy.

If a bias voltage is applied across the detector, the carriers will drift to the detector surfaces so they can be measured by ionisation sensors according to the Shockley- Ramo theorem. The additional potential energy transmitted to them by the applied voltage is released to the lattice via collisions (*Luke phonons*). Note that, in this case, the total phonon energy is larger than the recoil energy. An schematic representation of these

processes is shown in Fig. 3.1. All three kinds of phonons are collected by phonon sensors on the detector surface. This necessitates operation at low temperatures to reduce the noise from thermal phonons.

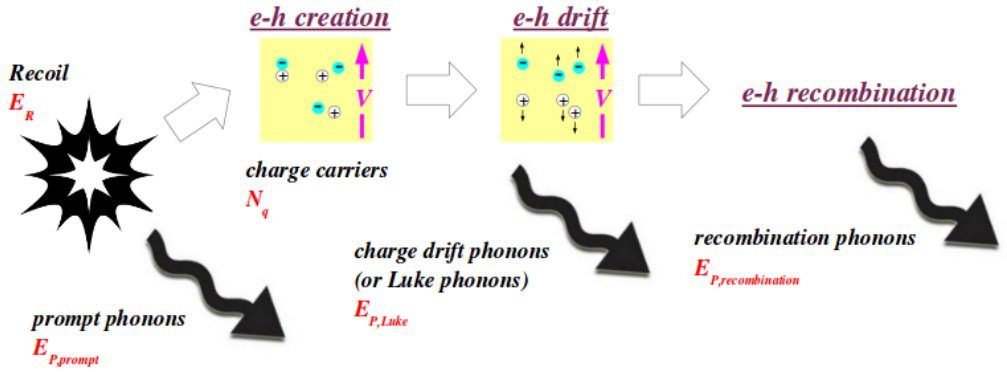

Figure 3.1: The three type of phonons produced in the interior of the crystal detectors [111].

The three phonons produced in the interaction have different characteristic frequencies. At low enough frequencies the mean free path of a phonon is greater than the size of the detector; these ballistic phonons travel fastest, at the speed of sound. Whereas, at higher frequencies scattering processes become important, slowing the phonon. The primary phonons produced by a particle interaction are mostly of the high-frequency type. However, eventually, those high-frequency phonons down-convert to ballistic phonons. Phonons generated by interactions which take place near the surface produce a faster signal.

3.2 SuperCDMS detectors

The SuperCDMS iZIP (interleaved Z-sensitive Ionization and Phonon) detectors measure ionisation and phonon energy simultaneously to distinguish WIMP candidate events from electromagnetic backgrounds. Each detector consists of a Ge crystal of diameter 76 mm and thickness 25 mm. Detectors are photolithographically patterned with interleaving phonon sensors grounded and ionisation sensors operated at +2V applied on the top face and -2V on the bottom face. This generates an electric field inside the detector as shown in Fig. 3.2. The phonon sensors consist of superconducting aluminium fins and tungsten Transition Edge Sensors (TESs). They are prepared to give four phonon readout channels on each detector face, one circular outer channel surrounding three inner channels. These sensors have been optimised to enhance the signal-noise ratio and provide excellent position information[112].

WIMPs and neutrons will produce NRs while electrons and photons will produce ERs. Events occurring near the surface can be identified by the asymmetry of their charge collection, thanks to the electric field.

The actual recoil energy can be recovered from the data by combining the information from the channels. The Luke phonon contribution, as determined from the ionisation channel information, is subtracted from the total phonon energy:

$$E_{recoil} = E_{phonon} - N_q e V_{bias}, \tag{3.1}$$

where N_q is the number of measured charge carriers.

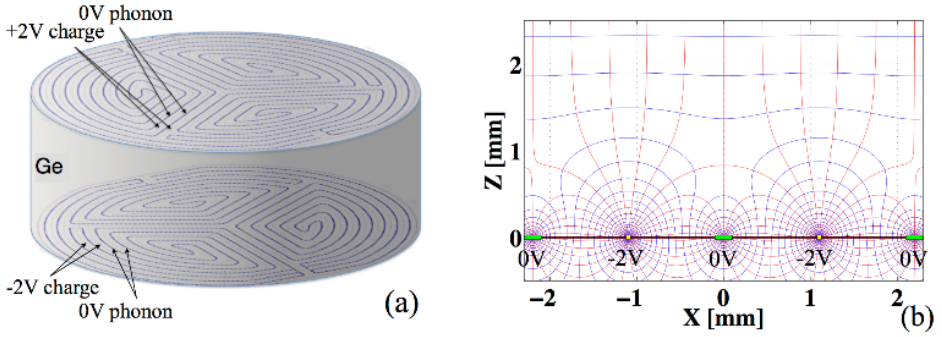

Figure 3.2: a. Phonon ionization sensor design for SuperCDMS iZIP detectors. b. Cross-sectional view of the electric field lines (red) and equipotential contours (blue) near the bottom face of a SuperCDMs iZIP detector. [113].

The proportion of the collision energy that is converted into ionisation is different for ERs and NRs. Thus, the collection of ionization and phonon information helps to extract recoil type easily. Recoil type is characterised by a derived quantity, ionization yield. This quantity is defined as the ratio of the measured ionisation signal to the total recoil energy, derived from both channels:

$$Y \equiv \frac{N_q \varepsilon}{E_{recoil}}, \tag{3.2}$$

where ε=3.0 eV for Ge. The ionisation yield is 1 for ERs and around 0.3 for NRs. This quantity is the basis for discrimination by recoil type.

Therefore, the combination of these last two equations allows obtaining the E_R and Y of every interaction, from the knowledge of the number of charge carriers, N_q, and the total phonon energy, E_p, only.

If an ER occurs very close to the detector surface, the ionisation yield is often not properly characterised. Surface events can then suffer from reduced ionisation collection, obtaining a value for the ionisation yield lower than one for ERs and then resembling NRs.

To aid identification of surface events the interleaving of the phonon and ionisation rails creates a complex electric field contracted at the surface of the detector. Events which deposit energy deeper than $\sim$ 1 mm will liberate charges that drift to both detector faces, while an event which interacts near the surface will generate a charge signal that is collected on only one of the detector faces. In addition, the outermost ionisation electrodes and phonon channel act as a veto guard ring to reject events originating on the perimeter of the detector.

Surface event discrimination and identification of events collected in the outer electrode allow the definition of an optimal FV and enable an efficient separation of surface and bulk events. The effective application of these cuts can be observed in Fig. 3.3.

3.3 Detector towers, cryogenics and shielding

The different layers which covers the detectors are divided into cryogenics, which allow to reach low temperatures, and the shielding, which protects the detectors of external background.

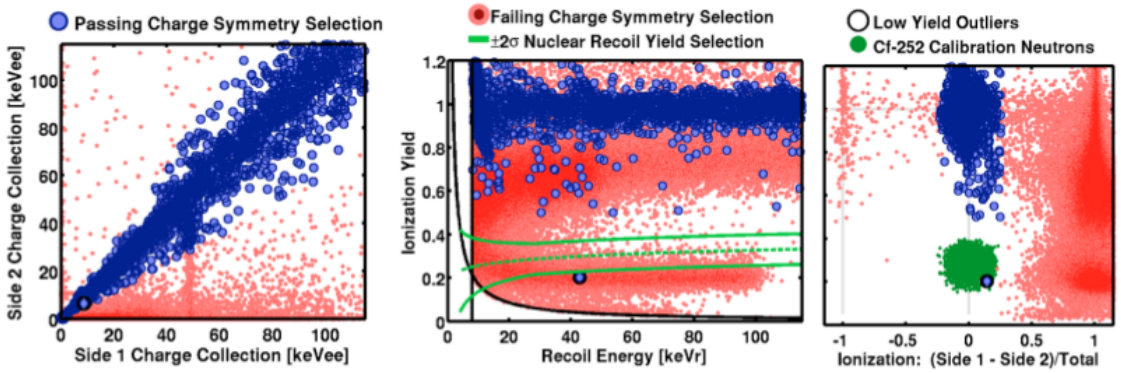

Figure 3.3: Left: Charge symmetry selection of bulk events in iZIP detector. Blue points pass the symmetry cut (approximately equal energy deposition on both sides of the detector); red points failed the charge symmetry selection (surface events). Middle: Iionization yield versus recoil energy of ^{133}Ba calibration data. One low yield outer is easily removed via application of a phonon symmetry cut. The green band shows the $\pm 2\sigma$ NR signal region, based on calibration data from ^{252}Cf. Right: Charge partition of ^{133}Ba events. ERs and surface events are well separated from the signal manifold. [114].

3.3.1 Detector towers and cryogenics

As it was explained in the previous section, to obtain a correct measure of the phonon energy operation at low temperatures is needed to reduce the noise of thermal phonons. Therefore, within the shield, the detector towers cryogenics consists of a set of concentric copper vessels cooled to the various temperature stages of the dilution refrigerator. These stages are room temperature (300 K), nitrogen shield (77 K), helium bath (4 K), still (∼1 K), cold plate (∼130 mK) and the mixing chamber.

Such low temperatures are achieved by an apparatus which refrigerates the detector towers, called the fridge. It allows to reach temperatures on the order of ∼50 mK. In addition, the cryocooler helps to achieve the operating temperature by setting an intermediate cryogenics stage. In Fig. 3.4, the fridge is showed in blue on the right side of the shielding. The C-stem connects this dilution refrigerator with the detector towers cryogenics, and the E-stem contains the read-out electronics.

Finally, the detector housings and bulk of the cold hardware inside the detector towers cryogenics are built with high-purity copper, to reduce the radioactive contamination close to the detectors. The total thickness of copper surrounding the detectors of few cm is enough to shield the detectors from α and β radiation from outside the vessels.

3.3.2 Shielding

SuperCDMS Soudan employs the same shielding setup previously used for CDMS II. It consists of an active shielding component to protect against residual cosmic-ray interactions and a passive component to shield against natural radioactivity.

Passive shielding

The passive shielding consists of three parts: an outer layer of polyethylene, two layers of lead and an inner layer of polyethylene, as shown in Fig. 3.4. To decide the order of the

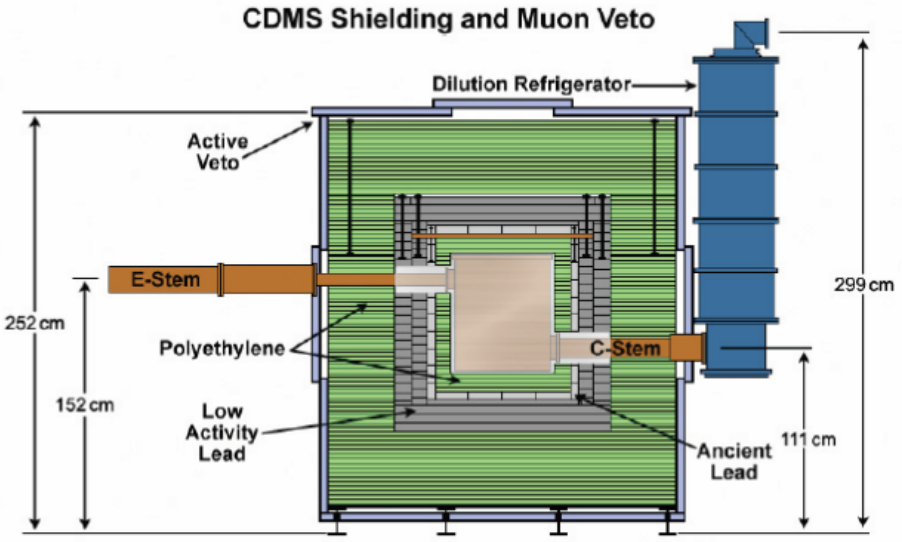

Figure 3.4: Schematic view of the side of the active veto and passive shielding for CDMS II and SuperCDMS. From the outside to the inside: muon veto panels (light blue), outer polyethylene shield (green), outer low radioactive lead shielding (gray) and mu-metal shield (light metal coloured). The E-stem and C-stem (brown) pass between the veto panels and the passive shielding connecting to the mu-metal shield. The C-stem connects to the dilution refrigerator (dark blue) providing the thermal contact between the cold layers and the fridge [15].

passive shielding, a Monte Carlo (MC) simulation was used to optimise the suppression of neutron background. The outer polyethylene layer is composed of one inch thick slabs surrounding the outer lead brick layer. The outer polyethylene layer is 40 cm thick on the sides and 40.6 cm thick at the top and bottom. The purpose of the outer polyethylene layer is to moderate the primary flux of neutrons from outside of the experimental apparatus down to energies that produce NRs below the detection thresholds of the detectors.

The lead shield is composed of inner and outer layers of lead surrounding the detectors cylindrically. Lead provides protection from ambient γ flux from natural radioactivity produced outside of the experimental apparatus. Outer and inner layers use different types of lead to obtain a better protection. The outer layer with a thickness of 17.8 cm on the top, bottom and sides and is composed of low-activity lead. On the other hand, the inner layer, employs ancient lead and it has a thickness of 4.4 cm on top, bottom and the sides. The ancient lead presents lower radioactivity because it does not contain the naturally occurring radioactive lead isotope ^{210}Pb. It is used to reduce the γ backgrounds due to radioactive isotopes in the outer lead.

The inner layer of polyethylene shielding is inside the inner ancient lead and provides further neutron moderation. It is 10 cm thick on the side, 7.6 cm thick on the top, and 10.2 cm thick at the bottom. The inner polyethylene reduces the cosmic-ray induced neutrons in the lead but without increasing the γ flux due to its not very large mass significantly.

The presence of magnetic fields can produce noise in the readout channels. To reduce the external magnetic field a can of mu-metal surrounds the detector within the inner polyethylene layer.

Active muon veto

The active veto consists of 40 plastic scintillator panels overlapping to surround the inner passive shielding. It is intended to reject the remaining muon flux not stopped by the rock overburden. Muons can produce neutrons when interacting with nuclei in the passive shielding, and the signal produced by neutrons is indistinguishable from the signature of WIMPs. The data acquired in the inner detector simultaneously to the muon event is discarded, so these scintillator panels act then as coincidence detectors to remove muon induced neutron background.

3.4 Data analysis

In this section, the techniques employed to analyse data in direct detection experiments, as well as the different analysis which have taken place in SuperCDMS Soudan are explained.

Let B denote the number of background events in the experiment; this number can be subtracted from the observed count rate. The accuracy of such a subtraction is limited by Poisson statistics giving an error on the subtraction of $\sigma_B = \sqrt{B}$. As the exposure increases $B \propto \epsilon$ and thus $\sigma_B \propto \sqrt{\epsilon}$; where, as mentioned in section 2.1, ϵ is the exposure with units are usually given in kg day. The number of excess candidate events needed to claim a detection scales as σ_B, so the experiments sensitivity grows only as $\sqrt{\epsilon}$ [15]. Note, however, that in absence of background the sensitivity would increase linearly with ϵ instead.

3.4.1 Blinding of the data

Searches looking for a signal from WIMP interactions in the detectors, define precise cuts on the event properties with the aim of selecting only events which satisfy the expected signal. In order to determine selection cuts in an unbiased way, a so-called "blind analysis" is carried out on the data set. This approach is based on removing all the events in the signal region from the data used to define the selection cuts, and then maintaining these events available only after that process is complete.

3.4.2 Building exclusion limits

Direct detection experiments are primarily counting experiments looking for a small number of NRs that arise independently from each other. Hence, the event counts will follow the Poisson statics. After running for a set period of time and after applying various cuts to reduce background events, a direct detection experiment reports the number of events n that are observed in a predefined energy range $[E_1, E_2]$. If no excess over the expected background is observed, an exclusion limit in the $m_\chi - \sigma_{WN}$ plane can be established. To set an exclusion limit at the 90% confidence level (C.L.). It is needed to find the Poisson parameter, μ, such that 90% of these experiments would have observed more than N events with the same exposure. Therefore, even if there is an absence of any excess in the direct detection experiment, it is possible to extract useful information to understand the nature of DM candidates.

For a given mass m_χ, the expected number of events N in a particular energy range is given by Eq. 2.5. The only free parameter that enters N is the cross section σ_{WN}. Thus, a limit on σ_{WN} can be calculated by setting $N = \mu$.

A detailed description of the three methods commonly used to establish an exclusion limit is presented in Appendix B of [115].

The first method, the 'Poisson method', is the simplest and tends to give the weakest limit. The other two methods, 'maximum gap' and 'p_{max}' work well in the presence of an unknown background. When no events are observed, they reduce to the Poisson method.

'Maximum gap' method reports a strong upper limit and it is commonly used to build the exclusion limits in direct detection experiments. It was already used in CDMS searches. This method can not be used to identify a positive detection. However, it is appropriate for obtaining upper limits from experiments whose backgrounds are poorly understood.

Maximum gap method

For a given WIMP mass and WIMP velocity distribution the shape of the distribution in E_{recoil} can be computed, but the WIMP cross section is unknown. In addition, backgrounds may be poorly understood, and the number of observed events may be too low to carry out a meaningful subtraction.

Each small rectangle in the horizontal axis of Fig. 3.5 represents events, including signal events, known background and possible unknown background events; with their corresponding energy. The smooth curve shows the event spectrum, dN/dE, expected from a proposed cross section, σ. This curve may also include known backgrounds. To establish the upper limit, the proposed size of σ is varied until it is high enough to be rejected as being too high. Therefore, it is necessary to seek criteria to consider a proposed signal is too high. The number of events is greater and low energies than at larger ones. Then, it is expected that more backgrounds events were situated at these low energies, and the calculation with the aim of obtaining a strongest upper limit must be done looking at higher energies where there are not many events, and therefore is not much background.

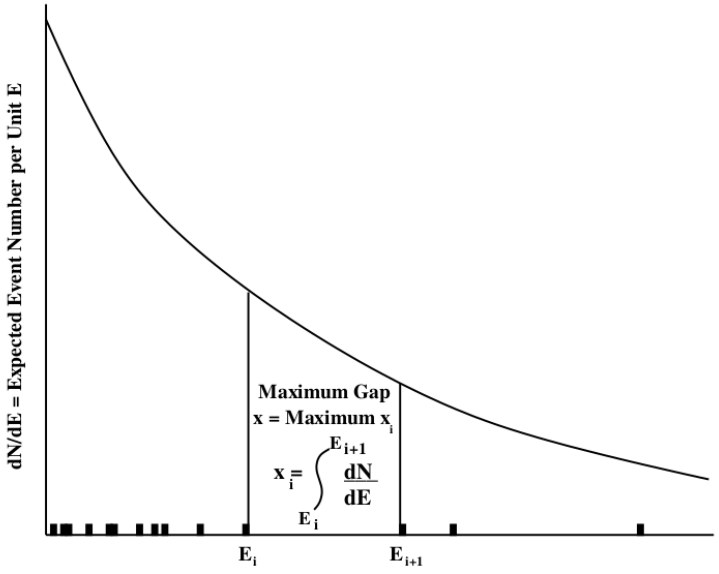

Figure 3.5: Illustration of the maximum gap method. The horizontal axis represents the energy measured for each event. The smooth curve represents the signal expected for a particular cross section, including any known background. The events originated from signal, known background and unknown background are the small rectangles along the horizontal axis. The integral of the signal between two events is "x_i" [116].

For any two events with energies E_i and E_{i+1}, and for a given value of σ, the size of

the gap between them can be characterised via integration:

$$x_i = \int_{E_i}^{E_{i+1}} \frac{dN}{dE} dE. \tag{3.3}$$

The maximum gap is the one with maximises this area under the curve. However, increasing the value of σ makes x_i bigger and bigger but it makes no sense to have millions of expected events in a region with null detection. Thus, a particular choice of σ should be rejected as too large if, with that choice, there is a gap between adjacent events with "too many" expected events. The selection for "too many" is that if the choice of σ were correct, a random experiment would almost always give fewer expected events in its maximum gap. Calling x to the size of the maximum gap in a random experiment, if this value x is lower than the observed maximum gap size with probability C_0, the considered x is rejected as too high with confidence level C_0. The value of x remains unchanged under one-to-one transformations of the variable in which events are distributed in the horizontal axis. Thus a transformation at a point is applied from E to a variable equal to the total number of events expected in the interval between the point and the lowest allowed value of the energy E. In this new variable, the expected number of events are distributed uniformly with unit density. Then any event distribution is equivalent to a uniform distribution of unit density. After applying the transformation, the total length of the distribution is equal to the expected total number of events, μ, without depending on the shape of the original event distribution. The probability, C_0, of the size of the maximum gap being smaller than a particular value of x is:

$$C_0(x, \mu) = \sum_{k=0}^{m} \frac{(kx - \mu)^k e^{-kx}}{k!} \left(1 + \frac{k}{\mu - kx}\right), \tag{3.4}$$

where m is the greatest integer $\leqslant \mu/x$. For a 90% confidence level upper limit, σ increases until μ and the observed x is such that $C_0 = 0 - 9$.

The derivation of Eq. 3.4 can be found in Appendix A of [116]. This method offers a conservative upper limit, and it excludes regions where a large unknown background causes events to be too close together for the maximum gap to be there.

3.4.3 Data analyses in SuperCDMS Soudan

In chronological order, the SuperCDMS experiment has provided the following results: 1) an analysis of the first test run using a novel phonon amplification technique (CDMSlite); 2) a low-mass WIMP search; and 3) an analysis of the second run using the CDMSlite technique. In addition, the SuperCDMS experiment is currently carrying out a WIMP search between 10 and 100 GeV/c^2.

First CDMSlite run

CDMSlite stands for *CDMS low ionisation threshold experiment*. This technique is based on amplifying the phonon signal produced by particles interacting with the detector, by using a bias voltage much larger than that used in nominal operation conditions. That enables to achieve lower energy thresholds and therefore allows to explore WIMP masses well below 10 GeV/c^2. In particular, the increased bias voltage applied amplifies the Luke contribution to the phonon signal,

$$E_P = E_R + N_q eV = E_R \left(1 + Y \frac{eV}{\epsilon}\right) = g(V) E_R. \tag{3.5}$$

Note that a factor of proportionality between the recoil energy and the total phonon energy, $g(V)$, is obtained, that is linear in V. Therefore, amplifying the voltage the phonon signal collected grows following this factor, thus effectively lowering the phonon energy threshold.

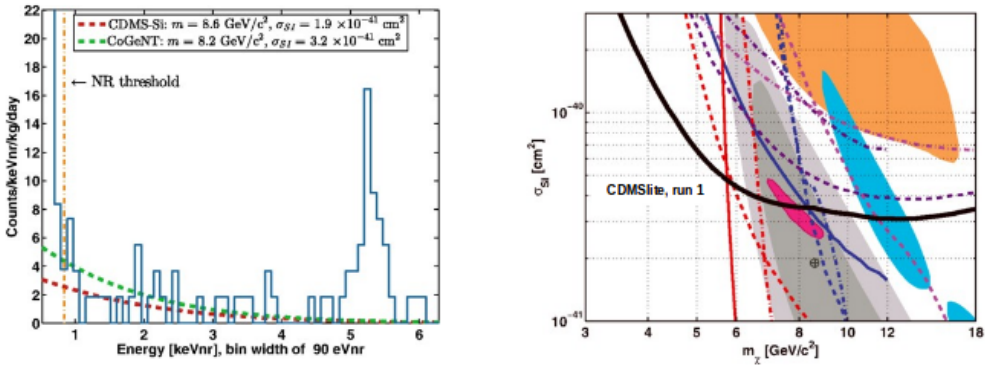

Figure 3.6: Results obtained by CDMSlite, run 1. Left: The efficiency-corrected WIMP-search energy spectrum is shown and compared with expected rates for WIMPs with the most likely masses and cross sections suggested by the analysis of CoGeNT (green, upper dashed curve) and CDMS II Si data (red, lower dashed curve). Right: 90% upper confidence limit from the data compared with the exclusion limits from other experiments. [117]

Note that this technique does not allow to amplify the ionisation signal, and therefore neither NR/ER discrimination or FV cuts are possible in CDMSlite.

The first test run was carried out using a single 0.6 kg Ge detector running for 10.3 live days in July 2012. The operating bias $V_b = 69$ V was chosen to optimise the signal-to-noise ratio. A threshold of 0.8 keV was reached, allowing to establish new constraints in the spin-independent parameter space for WIMPs with masses below 6 GeV/c^2. The results obtained by this analysis are presented in Fig. 3.6.

Low-mass WIMP search

The low-mass WIMP search [118] was the first analysis carried out with the full background rejection capabilities of SuperCDMS Soudan, in the limit of their resolution. Only the 7 detectors with lowest energy threshold were used, with a exposure of 577 kg days for WIMPs with masses <30 GeV/c^2, with the signal region blinded.

To select WIMP candidates, the triggered events were required to pass three levels of data-selection criteria: data quality, preselection, and event discrimination. The first level of criteria, data quality, rejects poorly reconstructed and noise-induced events. The second one, preselection, removes event configurations incompatible with WIMPs. Muon coincident events were rejected with a 98.7% of acceptance and also, multiple-scattering events. Events selected were also required to lie within the 3σ NR band and to pass fiducial volume cuts. The last event selection criteria was carried out using a multivariate analysis approach.

After applying these selection cuts, 11 events were observed. A new upper-limit on the spin-independent cross section was set, excluding new parameter space below 6 GeV/c^2, see Fig. 3.7. This result strongly disfavoured a WIMP-nucleon scattering interpretation of the excess reported by CoGeNT [119].

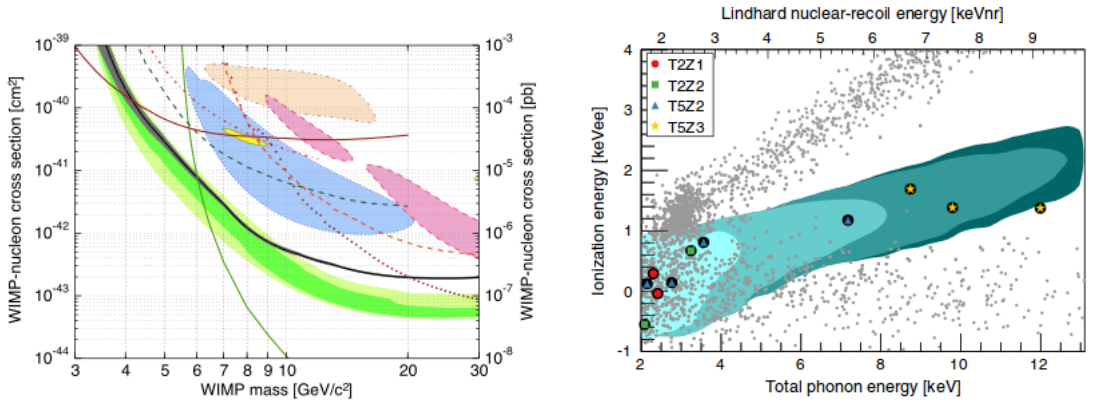

(a) (b)

Figure 3.7: Results for the low-mass WIMP search. (a). The 90% confidence upper limit (solid black) based on all observed events is shown with 95% C.L. systematic uncertainty band (gray). The preunblinding expected sensitivity in the absence of a signal is shown as 68and 95% (light green) C.L. bands. (b). Small gray dots are all veto-anticoincident single-scatter events within the ionization-partition FV that pass the data-quality selection criteria. Large encircled shapes are the 11 candidate events. [118]

Second CDMSlite run

This second run in CDMSlite [120] operation conditions was carried out following the successful results from the previous test run. The same detector was employed, taking data between February to November 2014, leading to a exposure of 70 kg day. A similar voltage of 70 V was applied to one side of the detector while keeping the other side at 0 V.

Several hardware and operational improvements were implemented with respect to the first run, reaching a 0.26-0.35 keV threshold. Unlike the first CDMSlite run, some event selection could be applied. First, pulse-shape was used to discriminate signal events from noise events, that allowed to lower the energy threshold below that for the first CDMSlite run. And second, a radial FV cut was developed, that lead to an increased sensitivity.

The use of this technique with the mentioned improvements made possible to exclude a new parameter space between 1.6-5.5 GeV/c^2. The results obtained are shown in Fig. 3.8.

WIMP search between 10 and 100 GeV/c^2

This analysis is currently being carried out. All ten fully functional detectors are being used, with ∼3000 kg days of exposure, collected between March 2012 and July 2014. This search allows to use the full background rejection capabilities. The signal region in recoil energy is situated between 2-100 keV. It uses a multivariate analysis to discriminate backgrounds. This analysis includes a detailed prediction of the irreducible neutron background from the environmental radioactivity, presented in the next chapter, that is the subject of the current dissertation.

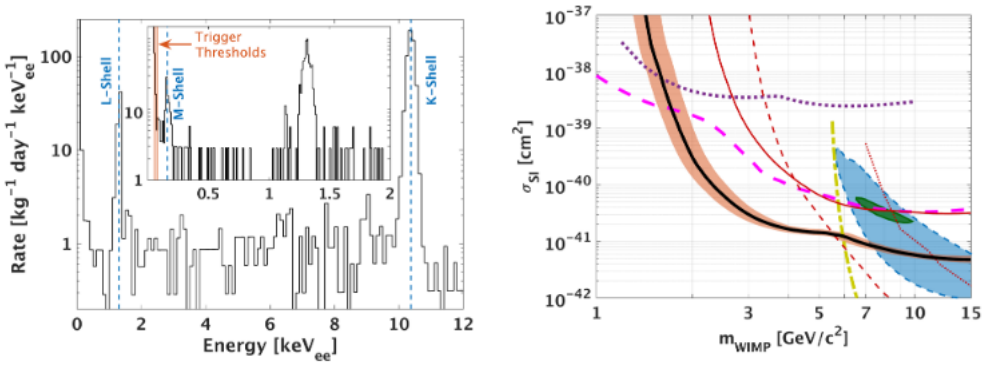

(a) (b)

Figure 3.8: Results obtained by CDMSlite, run 2. (a). Median (90% confidence level) and 95% interval of the WIMP limit from this analysis (black thick solid curve surrounded by salmon-shaded band) compared to other selected results. Other 90% upper limits shown are from the first CDMSlite run (red thin solid curve). [120]

3.5 SuperCDMS SNOLAB

The next generation SuperCDMS experiment will be a newly built experiment deployed at SNOLAB, in the Creighton Mine in Sudbury, Canada. The location provides 6010 m.w.e of overburden, reducing the fast neutron production significantly from cosmic-ray muons. SuperCDMS SNOLAB is expected to lead the search of WIMP below 10 GeV/c^2, as shown in Fig. 1.5.

In addition to Ge, also Si detectors will be employed. The crystal size of the detectors will be increased to 33 mm thickness and 100 mm diameter. Each Ge detector will have a mass of 1.39 kg, and each Si detector will have a mass of 0.6 kg. A new generation of iZIP detectors will be incorporated. On each side of the detectors, the number of phonon channels will increase from four to six, and two charge channels will be present. In addition, an important fraction of detectors will be operated in high-voltage (HV) mode biased at 100 V, analogous to the CDMSlite operation mode tested in SuperCDMS Soudan.

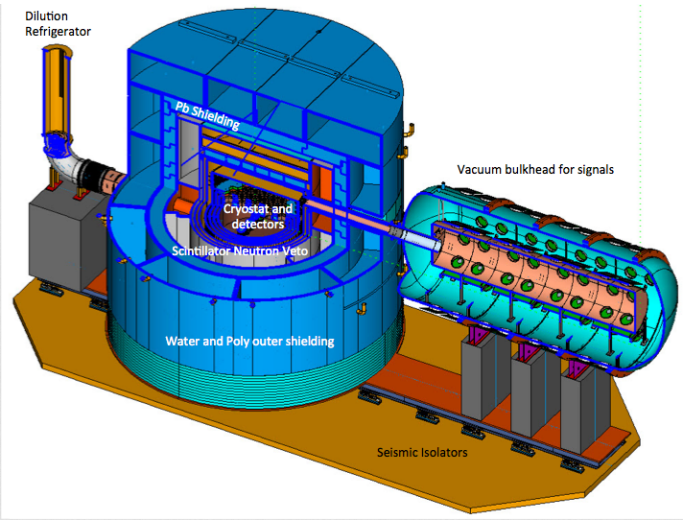

Figure 3.9: Shielding and cryostat proposed for SuperCDMS SNOLAB.

The experiment will consist of five towers with six detectors each. One tower will be devoted HV detectors running with four Ge detectors and two Si detectors. The other towers will be a mixture of Ge and Si detectors operating in nominal operation conditions. The towers will be housed in a ultrapure copper cryostat with capacity for 31 towers to allow for future upgrades. The configuration of the shielding will be based in the one employed in SuperCDMS Soudan. The cryostat will be surrounded by polyethylene layers to absorb neutrons emitted by radiogenic contaminants. Surrounding this inner polyethylene layer will be a layer of low activity lead, which will be surrounded by another layer of conventional lead, to block external γs. The lead layers will be surrounded by water tanks on a base of polyethylene to shield from external neutrons. The experiment will rest upon a seismic isolation platform to protect it from seismic events caused by mining activities. The shielding and cryostat proposed are showed in Fig. 3.9.

The initial payload will consist of 25 kg of iZIP Ge, 4.1 kg of iZIP Si, 5.6 kg of HV Ge and 1.4 kg of HV Si detectors. The HV detectors provide sensitivity to low-mass (<5 GeV/c^2) WIMPs while the iZIP detectors have superior sensitivity in intermediate mass ranges due to the background rejection capabilities. The construction of SuperCDMS SNOLAB is expected to be completed by 2020.

Chapter 4

Radiogenic neutron background in SuperCDMS Soudan

SuperCDMS Soudan detectors provide NR/ER discrimination and allow to define FV cuts. As explained in Chapter 3, these techniques can be used to reject a substantial part of the background from charged particles and γ-rays. However, an irreducible background contribution from neutrons is still expected to remain, on the order of 1 event per year or less. The current chapter explains the prediction of this background component from environmental radioactivity. This prediction will be compared with the number of single-scattering events measured in data, when unblinded. If there is a significant excess in the data collected in comparison with the simulated prediction that would indicate either and unexpected background or signal detection. Otherwise, and exclusion limit in the parameter space would be set.

This study is done in the context of the WIMP search between 10 and 100 GeV/c^2 being carried out currently in SuperCDMS, with a signal region of 2-100 keV. Two steps are necessary for this calculation. The first step is to measure the radioactive contamination levels in the experiment. Then, the second step is to simulate the propagation of the neutrons generated by the measured contaminants.

4.1 Radiogenic neutron sources in SuperCDMS Soudan

Neutrons with MeV energies can produce NRs at keV energies, the range of energy expected for WIMPs interactions. Radiogenic neutrons are generated by decay processes of radioactive materials near the detectors. Neutrons with kinetic energies up to 6 MeV can be produced either by spontaneous fission or (α, n) reactions [15],[121]. At the Soudan Underground Laboratory, ^{238}U and ^{232}Th exist in the rock surrounding the experimental cavern. ^{238}U contributes with neutrons generated by spontaneous fission and (α,n) reactions, whereas ^{232}Th decay chain only produces neutrons by the last process since the spontaneous fission rate is essentially negligible. Uranium and thorium spectra employed assume secular equilibrium. And the natural isotopes considered are ^{238}U and ^{232}Th.

The background from external neutrons crossing the full SuperCDMS shielding is considered to be negligible. Therefore, the radiogenic neutron background is expected to be dominated by the radioactive contamination within the shielding, namely the towers, the cryogenic copper vessels, and the innermost parts of the shielding.

4.2 Estimation of the contamination levels

To estimate the radiogenic neutron background, it is necessary to know the contamination levels of the different components of the innermost components which produce neutrons. γ-ray simulation provides information about which volumes contribute significantly to the radiogenic neutron background and which contributions can be considered negligible. Thus, from the results of this study, the distribution of the contaminants for the radiogenic neutron background is determined.

4.2.1 Gamma-ray simulation

The radioactive contamination levels in the experiment components within the shielding can be measured by γ-ray spectroscopy using WIMP-search data, since most of the events recorded by the experiment are ERs produced by γ-rays. A pure sample of γ-ray events was obtained by selecting bulk ER events between 20 keV and 3 MeV from WIMP-search data between March 2012 and May 2014. Only three detectors were considered, namely iT2Z1, iT2Z2 and iT4Z3. The measurement of the recoil energy was based on the ionisation signal only, assuming the ionisation yield for ERs to be equal to unity.

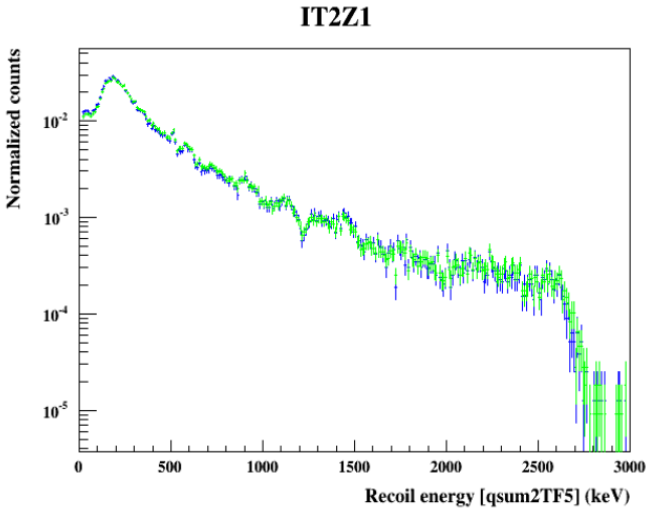

Figure 4.1: Energy spectrum, and chi-square of the charge pulse fit as a function of energy.

The information on the contaminant levels is mostly encoded in the peaks present in the γ-ray spectrum. The radioactive contaminants considered relevant in this analysis are shown in Table 4.1 and Table 4.2. All these contaminants were assumed to be distributed homogeneously in the bulk of the material. In addition, the distribution of the γ-ray rates over the detectors showed the existence of an intense γ-ray source below. Given that feature, this source is assumed to be due to radioactivity contamination from dust on top of some surface below the detectors. The most likely location for that type of contamination is the OVC, which is entirely exposed during towers assembly.

In order to obtain the contamination levels of any of these sources, MC simulations were performed to produce separate spectra for each isotope and each location. These simulations are carried out using Geant4 [122][123]. The MC simulations assume secular equilibrium and every volume was contaminated by separate in the bulk with ^{238}U and ^{232}Th, and their spectra are simulated, Fig. 4.1. The contamination levels are obtained from these MC simulations as follows.

The radioactive contaminants producing γ-ray photons can be classified into categories according to the decaying nuclides and their spatial distribution. Let $S(E)$ be the measured γ-ray spectrum, and $Si(E)$ the γ-ray spectrum, obtained from the MC simulation, that would be measured if only the category i were present [124]. Thus,

$$S(E) = \sum_i S_i(E). \tag{4.1}$$

The number of γ-ray events N_γ, is equal to the integral of the spectrum $S(E)$, and proportional to the total exposure. Introducing the associated probability density function $f(E)$ and $f_i(E)$, defined by normalizing $S(E)$ and $S_i(E)$ respectively to unity, previous equation can be written as:

$$f(E) = \sum_i w_i f_i(E), \tag{4.2}$$

where w_i is the relative contribution of category i to N_γ. If the radioactive contaminants from category i are assumed to be distributed uniformly over a definite volume V_i, the radioactivity per unit volume ρ_i satisfies the following relation:

$$w_i N_\gamma = \alpha_i \rho_i V_i L, \tag{4.3}$$

where α_i is the fraction of γ decays in the volume V_i for which the photon deposits energy in the detector, and L is the live time. Then,

$$\rho_i = \frac{w_i N_\gamma}{\alpha_i V_i L}. \tag{4.4}$$

In the case of radioactive contaminants distributing uniformly over a definite surface the equation is:

$$\sigma_i = \frac{w_i N_\gamma}{\alpha_i A_i L}, \tag{4.5}$$

where σ_i is the radioactivity per unit area and A_i is the area of the considered surface.

Based on the considerations above, the radioactivity levels can be obtained as follows. First, N_γ and $f(E)$ are obtained by selecting a pure sample of γ-ray events from data. Later, $fi(E)$ and α_i are calculated from MC simulations, for each category i. Finally, the weights w_i are obtained using a minimisation procedure, and the equations 4.4 and 4.5 are applied.

The values for the contaminants relevant for radiogenic neutron background estimation are presented in Table 4.1.

Table 4.1: Radioactivity levels of the different volumes which contribute to the bulk contamination.

Contaminant	**Activity** (mBq/kg)
^{232}Th, Towers	1.4(-0.4, +0.4)
^{238}U, Towers	< 2.07
^{232}Th, Cryogenic copper vessels	< 0.19
^{238}U, Cryogenic copper vessels	< 0.27
^{232}Th, Inner Polyethylene	1.5 (-0.5, +0.5)
^{238}U, Inner Polyethylene	0.59 (-0.39, +0.39)

In addition to the OVC, contamination on other surfaces were considered. In each case, the spectrum was simulated separately and compared with the data collected to obtain

Table 4.2: Radioactivity levels of the different volumes which contribute to the surface contamination.

Contaminant	**Activity** (mBq/cm^2)
^{232}Th, OVC bottom surface	1.8 (-0.19, +0.4)
^{238}U, OVC bottom surface	1.1 (-0.9, +0.9)

which configuration offered the best fit. Finally, it was decided that only the OVC surface contribution would be considered for two main reasons. The first one is that it offered the best fit to the measured spectra. The second one is that the other configurations entailed surface contaminated further away from the detectors. Then the neutrons produce by them would be moderated by the shielding and would reach the detectors in less proportion. As the experiment is looking for an excess over the expected background, it is better to adopt a conservative approach with the aim of avoiding a false positive detection by predicting less background. Therefore is better to consider the configuration which will contribute with more neutrons.

4.3 Radiogenic neutron simulation

The radioactivity levels obtained in the previous section are used here to calculate the radiogenic neutron background, using a simulation to propagate the neutrons and then calculate the rate at which radiogenic neutrons produce a WIMP-like signal in the detectors. These simulations are also carried out using Geant4. This calculation used the same isotopes and locations, as for the measurement of the radioactivity levels.

The MC events are selected considering single-scattering events in a signal region between 2-100 keV. Once the number of events which pass these cuts is obtained, the acceptance, α, can be calculated. The acceptance is defined as the number of events selected divided by the total number of events generated in the simulation. When this value is known for the different isotopes and locations, the radiogenic neutron background, N, can be estimated by multiplying the neutron rate, R_n, by this acceptance, α, together with the live time of each detector, L.

$$N = \alpha \cdot L \cdot R_n, \tag{4.6}$$

This study uses the 10 fully functional detectors considered in the WIMP-search between 10 and 100 GeV/c^2, with a total exposure of ∼1694 kg day. The study was done for each of the detectors separately due to their different response and also their various live times. As it was defined previously, the live time is the total amount of time in which detectors are prepared to detect a WIMP. For a period of data taking this is real time minus the intervals over which events are being recorded. It is readjusted considering if periods of data taking were rejected due to high noise or other problems. The list of the detectors considered and their corresponding live time is presented in Table 4.3.

4.3.1 Simulation

The neutron spectrum used for ^{238}U contribution takes into account the (α,n) reactions and the spontaneous fission. For ^{232}Th contribution, the neutron spectrum only considers (α,n) reactions.

The analysis must be done separately for every of the 10 detectors considered in the study. Firstly, the spectrum is generated for every detector and contaminant, Fig. 4.2.

Table 4.3: Live times for any detector used in the calculation.

Detector	Live time (day)
iT1Z1	285.73
iT2Z1	317.29
iT2Z2	322.37
iT2Z3	313.15
iT3Z1	206.01
iT3Z2	307.77
iT3Z3	210.58
iT4Z2	322.84
iT4Z3	347.52
iT5Z2	144.83

Posteriorly, neutrons which interact in the signal region are selected. The ones which interact simultaneously in more than one detector are disregarded. Then, comparing the total number of single-scattering neutrons obtained in the simulation with the total number of neutron generated the acceptance, α, can be calculated, Table 4.4.

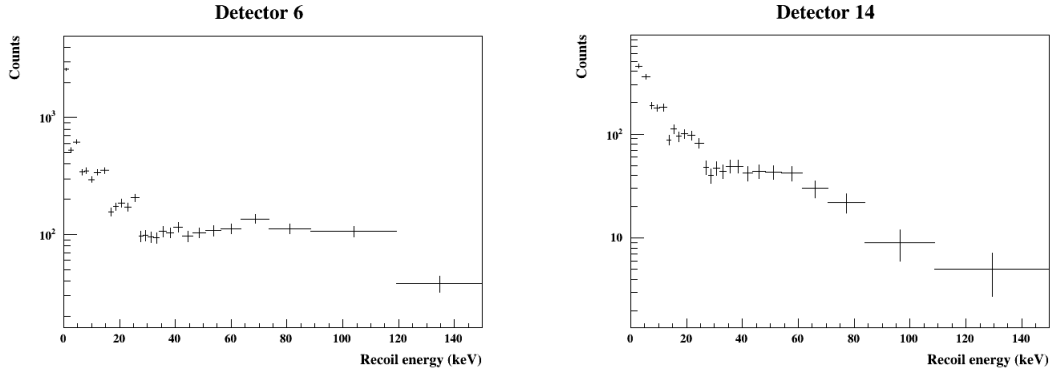

(a) (b)

Figure 4.2: Two spectra obtained for bulk and surface contamination. (a). ^{238}U spectrum for the inner bottom surface of the OVC. (b). ^{232}Th spectrum for the inner polyethylene.

For the surface contamination, the calculation of the acceptance requires to select MC events generated only on the top of the bottom OVC lid. To that purpose, a cut was applied to events with primary vertex below -0.285 m, checked with the simulation to. The rest of the analysis is the same that was done for the bulk events.

Table 4.4: Number of events simulated for every considered volume.

Volume	Number of events
Cryogenic copper vessels	10^7
Inner Polyethylene	10^6
Towers	$5{\cdot}10^5$
Inner surface OVC	10^7

As a check, the position of the primary vertices was simulated. The primary vertices show the exact place where the neutron is generated. The objective of this test is to be

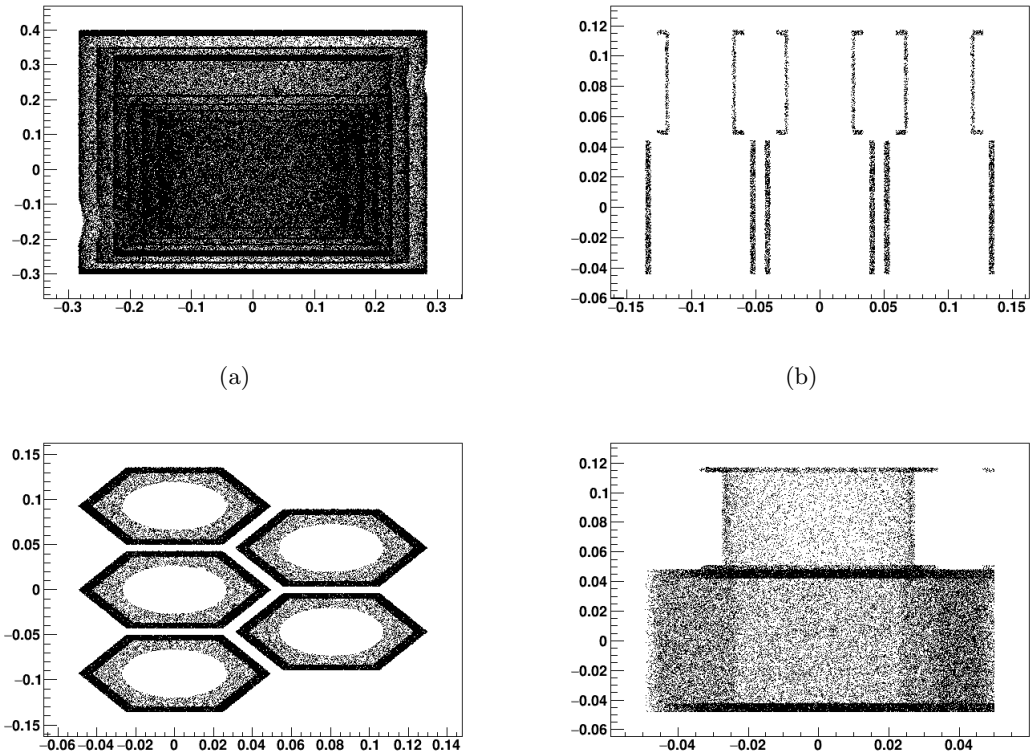

(a) (b)

(c) (d)

Figure 4.3: (a). Detector towers cryogenics contaminated with ^{232}Th. (b). Interior of the tower housing contaminated with ^{232}Th, XZ plane. (c). Stage 2 of the towers contaminated with ^{238}U, XY plane. (d). Exterior of the tower housing contaminated with ^{238}U, XZ plane.

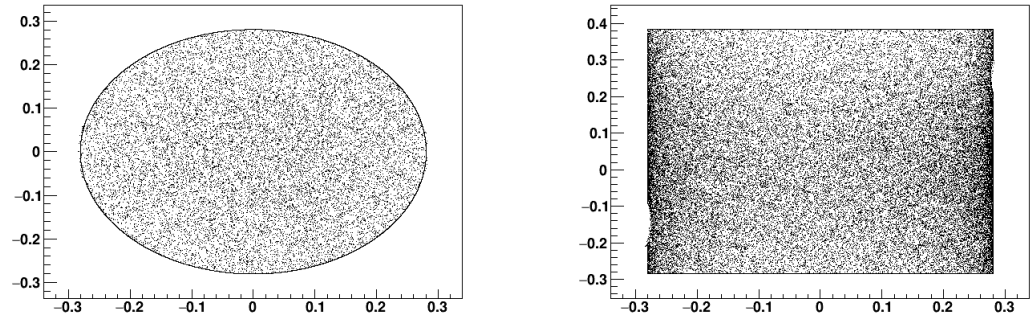

(a) (b)

Figure 4.4: Primary vertices of the surface contamination of the OVC, using ^{238}U spectrum. (a). XY plane. (b). XZ plane.

sure that the configuration of the contaminants in the simulation was done properly and that the materials contaminated corresponded with the ones selected in the γ-ray study. Figures 4.3 and 4.4 show the position of the primary vertices for different isotopes and

locations.

4.3.2 Results

Following Eq.4.6, the acceptance is multiplied by the neutron production rate and the live time in order to obtain the radiogenic neutron background. Both the acceptance and the live time depend on the detector. The product of these two quantities is shown in Table 4.7.

To carry out the calculation, it is necessary to know the neutron production rate, R_N, of every volume configuration considered in the study. This neutron rate can be obtained by considering the neutron yield, Y_n, which is defined as the rate of neutrons produced per unit of volume per concentration of mass of contaminant, expressed in ppb . The neutron yield depends just on the material and the values employed for the calculation are presented in Table 4.5.

Table 4.5: Neutron Yields (n/s cm^{3}ppb).

Source Material	**Polyethylene**	**Copper**
^{238}U	2.59 10^{-11}	1.238 10^{-10}
^{232}Th	5.28 10^{-12}	9.49 10^{-12}

To obtain the neutron production rate, it is necessary to multiply the product of the neutron yield and the concentration of contamination levels by the volume of the contaminant. In the case of the surface contamination, this quantity is multiply by the area and divided by the density.

$$R_{n,bulk} = Y_n\, V\, K. \tag{4.7}$$

$$R_{n,surface} = Y_n\, \frac{S}{d}\, K. \tag{4.8}$$

Where V is the volume and S the area of the sources, d the density and K is the concentration of contaminant. The density employed to obtain the neutron production rate for the surface contamination was the one of the copper; $d = 8.93$ g/cm^3. This choice is based on assuming that the surface contaminants are composed of particles small with respect to the mean free path of α particles ($\sim \mu$m), and therefore the (α,n) reaction takes place in the copper near the contaminant. The density which must appear in equation 4.8 is the one of the material the neutrons produced in the dust interact with. The areas and volumes considered were obtained using the geometric configuration of the simulation for the different cryogenic copper vessels and the towers. In the case of the inner polyethylene, the simulation provides information about the density of the polyethylene employed and the mass, so the volume can be calculated.

K is proportional to the radioactivity levels obtained with the γ-ray simulation.

$$K = \lambda\, A. \tag{4.9}$$

A is the contamination level of the source, and λ is a proportionality factor. The value of λ differs for ^{238}U and for ^{232}Th, and their exact values are expressed in Table 4.6.

To obtain the total radiogenic neutron background the neutron production rate has to be multiplied by the live time and the acceptance. As such product is different for every detector the value $\alpha \cdot t$, where t is the live time, was obtained for every detector and

Table 4.6: Proportionality factor, λ .

Source Material	$1/\lambda \left(\frac{mBq/kg}{ppb}\right)$
^{238}U	12
^{232}Th	4.1

summed up to obtain a value for every contaminant. The results obtained are presented in Table 4.7.

Table 4.7: Acceptance multiplied by live time for every contaminant.

Contaminant	$\alpha \cdot L$ **(s)**
^{232}Th, Cryogenic copper vessels	103022±792
^{238}U, Cryogenic copper vessels	75803±594
^{232}Th, Towers	517749±4264
^{238}U, Towers	438801±3696
^{232}Th, Inner Polyethylene	10509±136
^{238}U, Inner Polyethylene	5985±96
^{232}Th, OVC bottom surface	17089±190
^{238}U, OVC bottom surface	27063±269

Using all of the already mentioned quantities the radiogenic neutron background for every volume and contribution was obtained. The resulting values together with the correspondent uncertainties are shown in Table 4.8. The process followed to obtains these uncertainties will be explained in detail in the next section.

Table 4.8: Number of single-scattering neutrons for any of the volumes considered.

Contaminant	**Number of single-scattering neutrons** $(\cdot 10^{-2})$
^{232}Th, Cryogenic copper vessels	<0.07
^{238}U, Cryogenic copper vessels	<0.3
^{232}Th, Towers	$0.25^{+0.07}_{-0.07}$
^{238}U, Towers	<2.1
^{232}Th, Inner Polyethylene	$0.5^{+0.2}_{-0.2}$
^{238}U, Inner Polyethylene	$0.2^{+0.1}_{-0.1}$
^{232}Th, OVC bottom surface	$1.9^{+0.4}_{-0.2}$
^{238}U, OVC bottom surface	5^{+5}_{-4}

It is observed that the largest contribution to the radiogenic neutron backgrounds comes from the surface contamination.

To compute the total value of the radiogenic neutron background it is necessary to sum up all of the various contributions together with the proper propagation of errors. The final result was: $N = 0.095^{+0.06}_{-0.05}$, the calculation of the uncertainties is discussed in the next subsection. This value is in correct agreement with the initial guess of expected events to be less than unity.

4.3.3 Propagation of uncertainties

Some quantities involved in the calculation of the radiogenic neutron background have associated systematic and/or statistics uncertainties. Though the propagation of statistical

uncertainties has well-defined procedures, there is not a generic approach to propagate systematic uncertainties and combine them with the statistical ones.

On one hand, statistical uncertainties are the result of stochastic fluctuations arising from the fact that a measurement is based on a finite number of observations. Therefore, repeated measurements of the same phenomenon will give rise to a set of results which will differ, and the statistical uncertainty is a measure of the range of this variations. The dominant sources of statistical uncertainty in this study have been identified to be the radioactivity levels and the neutron acceptances obtained from MC simulations. The results shown in Table 4.8, include the statistical uncertainties in the acceptances of the detectors and the radioactivity levels. The volumes, areas, neutron yields and density employed in the final calculation are considered to have negligible statistical uncertainty. Therefore, considering just the uncertainties introduced by the acceptances and radioactivity levels, the statistical errors were added in quadratures.

On the other hand, systematic uncertainties arise from the lack of knowledge on some parts of the analysis [125], for example, model parameters or apparatus performance, that requires introducing assumptions with an associated uncertainty. In this work the dominant source of systematic uncertainty has been identified to be the differences in detector response, that affect the measurement of the radioactivity levels. This uncertainty is assessed by calculating the variation of the result when one of the detectors used for calculating the contaminant levels is removed. Two cases were considered: one removing iT2Z1, and another removing iT2Z2. The case of removing iT4Z3 is not considered as it provides most of the sensitivity to the dominant contaminant source. Then, this uncertainty is propagated to the final result by repeating in each case the process explained in Subsec. 4.3.2, and then calculating the difference with respect to the central value calculated there.

The final statistical and systematic uncertanties are combined by adding both arithmetically.

Bibliography

[1] E. Hubble. and M. L. Humason. *The Velocity-Distance Relation among Extra-Galaxtic Nebulae. Astrophys*, 1931.

[2] F. Zwicky. *Die Rotverschiebung von extragalaktischen Nebeln. Helvetica Physica Acta*, 6:110–127, 1933.

[3] F. Zwicky. *On the masses of nebulae and of clusters of nebulae. Astrophysical*, 1937.

[4] P. A. R. Ade et al. *Planck 2015 results. XIII. Cosmological parameters*. 2015.

[5] M. C. Weisskopf et al. *An Overview of the performance of the Chandra X-Ray Observatory. Exper. Astron.*, 16:1–68, 2003.

[6] F. Jansen et al. *XMM-Newton observatory. I. The spacecraft and operations. Astron. Astrophys.*, 365:L1–L6, 2001.

[7] R. Narayan and M. Bartelmann. *Lectures on gravitational lensing*. In *13th Jerusalem Winter School in Theoretical Physics: Formation of Structure in the Universe Jerusalem, Israel, 27 December 1995 - 5 January 1996*, 1996.

[8] D. Clowe et al. *A direct empirical proof of the existence of dark matter. Astrophys. J.*, 648:L109–L113, 2006.

[9] Vera C. Rubin and W. K. Ford. *Rotation of the Andromeda Nebula from a Spectroscopic Survey of Emission Regions. Astrophys. J.*, 159:379–403, 1970.

[10] *The Early Universe*. Westview Press, 1990.

[11] T. Padmanabhan. *Structure Formation in the Universe*. Cambridge University Press, 1993.

[12] S. Dodleson. *Modern Cosmology*. Academic Press, 2003.

[13] R. A. Alpher, H. Bethe, and G. Gamow. *The Origin of Chemical Elements. Phys. Rev.*, 73:803–804, Apr 1948.

[14] R. H. Cyburt, B. D. Fields, and K. A. Olive. *Primordial nucleosynthesis in light of WMAP. Phys. Lett.*, B567:227–234, 2003.

[15] T. Bruch. *A Search for Weakly Interacting Particles with the Cryogenic Dark Matter Search Experiment*. PhD thesis, Universität Zürich, 2010.

[16] S. D. McDermott, H. Yu, and K. M. Zurek. *Turning off the Lights: How Dark is Dark Matter? Phys. Rev.*, D83:063509, 2011.

[17] C. Kouvaris. *Composite Millicharged Dark Matter*. *Phys. Rev.*, D88(1):015001, 2013.

[18] A. D. Dolgov, S. L. Dubovsky, G. I. Rubtsov, and I. I. Tkachev. *Constraints on millicharged particles from Planck data*. *Phys. Rev.*, D88(11):117701, 2013.

[19] E. Del Nobile, M. Nardecchia, and P. Panci. *Millicharge or Decay: A Critical Take on Minimal Dark Matter*. *JCAP*, 1604(04):048, 2016.

[20] N. Arkani-Hamed, S. Dimopoulos, and G. R. Dvali. *The Hierarchy problem and new dimensions at a millimeter*. *Phys. Lett.*, B429:263–272, 1998.

[21] L. Randall and R. Sundrum. *A Large mass hierarchy from a small extra dimension*. *Phys. Rev. Lett.*, 83:3370–3373, 1999.

[22] M. Pospelov, A. Ritz, and M. B. Voloshin. *Bosonic super-WIMPs as keV-scale dark matter*. *Phys. Rev.*, D78:115012, 2008.

[23] I. F. M. Albuquerque and L. Baudis. *Direct detection constraints on super-heavy dark matter*. *Phys. Rev. Lett.*, 90:221301, 2003. [Erratum: Phys. Rev. Lett.91,229903(2003)].

[24] J. Park and S. C. Park. *Superheavy Dark Matter in Light of Dark Radiation*. *J. Korean Phys. Soc.*, 65:805–808, 2014.

[25] G. Bertone and D. Hooper. *A History of Dark Matter*. *Submitted to: Rev. Mod. Phys.*, 2016.

[26] S. Dodelson and L. M. Widrow. *Sterile-neutrinos as dark matter*. *Phys. Rev. Lett.*, 72:17–20, 1994.

[27] P. P. Avelino and D. Barbosa. *Scaling defect decay and the reionization history of the Universe*. *Phys. Rev.*, D70:067302, 2004.

[28] D. Gorbunov, A. Khmelnitsky, and V. Rubakov. *Constraining sterile neutrino dark matter by phase-space density observations*. *JCAP*, 0810:041, 2008.

[29] L. D. Duffy and K. van Bibber. *Axions as Dark Matter Particles*. *New J. Phys.*, 11:105008, 2009.

[30] R. D. Peccei and H. R. Quinn. CP *Conservation in the Presence of Pseudoparticles*. *Phys. Rev. Lett.*, 38:1440–1443, Jun 1977.

[31] R. D. Peccei and H. R. Quinn. *Constraints imposed by* CP *conservation in the presence of pseudoparticles*. *Phys. Rev. D*, 16:1791–1797, Sep 1977.

[32] S. Weinberg. *A New Light Boson?* *Phys. Rev. Lett.*, 40:223–226, Jan 1978.

[33] F. Wilczek. *Problem of Strong P and T Invariance in the Presence of Instantons*. *Phys. Rev. Lett.*, 40:279–282, Jan 1978.

[34] G. Steigman and M. S. Turner. *Cosmological constraints on the properties of weakly interacting massive particles*. *Nuclear Physics B*, 253:375 – 386, 1985.

[35] G. Jungman, M. Kamionkowski, and K. Griest. *Supersymmetric Dark Matter*. *Phys. Rept.*, 267:195–373, 1996.

[36] A. Falvard et al. *Supersymmetric dark matter in M31: can one see neutralino annihilation with celeste? Astropart. Phys.*, 20:467–484, 2004.

[37] G. Bertone, D. Hooper, and J. Silk. *Particle dark matter: Evidence, candidates and constraints*. *Phys. Rept.*, 405:279–390, 2005.

[38] C. Csaki. *The Minimal supersymmetric standard model (MSSM)*. *Mod. Phys. Lett.*, A11:599, 1996.

[39] F. D. Steffen. *Dark Matter Candidates - Axions, Neutralinos, Gravitinos, and Axinos*. *Eur. Phys. J.*, C59:557–588, 2009.

[40] T. Falk, K. A. Olive, and M. Srednicki. *Heavy sneutrinos as dark matter*. *Phys. Lett.*, B339:248–251, 1994.

[41] J. A. R. Cembranos, J. L. Feng, A. Rajaraman, and F. Takayama. *Gravitino and axino superWIMPs*. *AIP Conf. Proc.*, 903:591–594, 2007. [,591(2007)].

[42] M. Cirelli. *Status of Indirect (and Direct) Dark Matter searches*. 2015.

[43] H. Silverwood. *Determining the Local DM Density*. In *PoS ICRC 2015*.

[44] M. Duranti. *Precision Measurement of the $(e^+ + e^-)$ Flux in Primary Cosmic Rays from 0.5 GeV to 1 TeV with the Alpha Magnetic Spectrometer on the International Space Station*. *Phys. Rev. Lett.*, 113:221102, Nov 2014.

[45] O. Adriani et al. *PAMELA results on the cosmic-ray antiproton flux from 60 MeV to 180 GeV in kinetic energy*. *Phys.Rev.Lett.105:121101,2010*.

[46] F. Donato, N. Fornengo, and P. Salati. *Anti-deuterons as a signature of supersymmetric dark matter*. *Phys. Rev.*, D62:043003, 2000.

[47] H. Fuke et al. *Search for cosmic-ray antideuterons*. *Phys. Rev. Lett.*, 95:081101, 2005.

[48] P. von Doetinchem, T. Aramaki, C. J. Hailey, S. Boggs, H. Fuke, S. I. Mognet, R. A. Ong, J. Zweerink, and K. Perez. *GAPS - Dark matter search with low-energy cosmic-ray antideuterons and antiprotons*. *PoS*, ICRC2015:1219, 2015.

[49] J. Carr et al. *Prospects for Indirect Dark Matter Searches with the Cherenkov Telescope Array (CTA)*. In *Proceedings, 34th International Cosmic Ray Conference (ICRC 2015)*, 2015.

[50] J. P. Harding and B. Dingus. *Dark Matter Annihilation and Decay Searches with the High Altitude Water Cherenkov (HAWC) Observatory*. In *Proceedings, 34th International Cosmic Ray Conference (ICRC 2015)*, 2015.

[51] G. Di Sciascio. *The LHAASO experiment: from Gamma-Ray Astronomy to Cosmic Rays*. In *Cosmic Ray International Seminar: The status and the future of the UHE Cosmic Ray Physics in the post LHC era (CRIS 2015) Gallipoli, Italy, September 14-16, 2015*, 2016.

[52] L. Goodenough and D. Hooper. *Possible Evidence For Dark Matter Annihilation In The Inner Milky Way From The Fermi Gamma Ray Space Telescope*. 2009.

[53] T. Daylan, D. P. Finkbeiner, D. Hooper, T. Linden, S. K. N. Portillo, N. L. Rodd, and T. R. Slatyer. *The characterization of the gamma-ray signal from the central Milky Way: A case for annihilating dark matter*. *Phys. Dark Univ.*, 12:1–23, 2016.

[54] M. G. Aartsen et al. *Multipole analysis of IceCube data to search for dark matter accumulated in the Galactic halo. European Physical Journal C 01/2015; 75(20).*

[55] S. Adrian-Martinez et al. *Search of Dark Matter Annihilation in the Galactic Centre using the ANTARES Neutrino Telescope*. *JCAP*, 1510(10):068, 2015.

[56] P. Cushman et al. *Working Group Report: WIMP Dark Matter Direct Detection*. In *Community Summer Study 2013: Snowmass on the Mississippi (CSS2013) Minneapolis, MN, USA, July 29-August 6, 2013*, 2013.

[57] K. Martens. *The XMASS Experimental Program and its Current Implementation*. *PoS*, ICRC2015:1214, 2016.

[58] E. Aprile et al. *Physics reach of the XENON1T dark matter experiment*. *JCAP*, 1604(04):027, 2016.

[59] D. S. Akerib et al. *First Results from the LUX Dark Matter Experiment at the Sanford Underground Research Facility. Phys. Rev. Lett.*, 112:091303, Mar 2014.

[60] J. Xu et al. *A Study of the Residual ^{39}Ar Content in Argon from Underground Sources*. *Astropart. Phys.*, 66:53–60, 2015.

[61] K. Rielage et al. *Update on the MiniCLEAN Dark Matter Experiment*. *Phys. Procedia*, 61:144–152, 2015.

[62] P. A. Amaudruz et al. *DEAP-3600 Dark Matter Search*. In *Proceedings, 37th International Conference on High Energy Physics (ICHEP 2014): Valencia, Spain, July 2-9, 2014*, volume 273-275, pages 340–346, 2016.

[63] P. Agnes et al. *First Results from the DarkSide-50 Dark Matter Experiment at Laboratori Nazionali del Gran Sasso*. *Phys. Lett.*, B743:456–466, 2015.

[64] T. A. Girard et al. *Girard and others for the SIMPLE Collaboration Reply:*. *Phys. Rev. Lett.*, 108:259002, Jun 2012.

[65] M. Felizardo et al. *The SIMPLE Phase II Dark Matter Search*. *Phys. Rev.*, D89(7):072013, 2014.

[66] E. Behnke et al. *First Dark Matter Search Results from a 4-kg CF_3I Bubble Chamber Operated in a Deep Underground Site*. *Phys. Rev.*, D86(5):052001, 2012. [Erratum: Phys. Rev.D90,no.7,079902(2014)].

[67] C. Amole et al. *Improved dark matter search results from PICO-2L Run 2*. *Phys. Rev.*, D93(6):061101, 2016.

[68] R. Bernabei et al. *New results from DAMA/LIBRA*. *The European Physical Journal C*, 67(1):39–49, 2010.

[69] R. Bernabei et al. *Particle Dark Matter in DAMA/LIBRA*. 2010.

[70] J. Amare et al. *Status of the ANAIS Dark Matter Project at the Canfranc Underground Laboratory*. In *Proceedings, 11th Patras Workshop on Axions, WIMPs and WISPs (Axion-WIMP 2015): Zaragoza, Spain, June 22-26, 2015*, 2015.

[71] K. Kim. *Status of the KIMS-NaI experiment*. In *Proceedings, Meeting of the APS Division of Particles and Fields (DPF 2015): Ann Arbor, Michigan, USA, 4-8 Aug 2015*, 2015.

[72] K. Fushimi et al. *Dark matter search project PICO-LON*. *J. Phys. Conf. Ser.*, 718(4):042022, 2016.

[73] W. C. Pettus. *DM-Ice: Current Status and Future Prospects*. In *Proceedings, 12th Conference on the Intersections of Particle and Nuclear Physics (CIPANP 2015): Vail, Colorado, USA, May 19-24, 2015*, 2015.

[74] K. Freese A. K. Drukier and D. N. Spergel. *Detecting cold dark-matter candidates. Phys. Rev. D*, 33:3495–3508, Jun 1986.

[75] E. Daw et al. *The DRIFT Directional Dark Matter Experiments*. *EAS Publ. Ser.*, 53:11–18, 2012.

[76] K. Nakamura et al. *NEWAGE - Direction-sensitive Dark Matter Search Experiment*. *Phys. Procedia*, 61:737–741, 2015.

[77] C. Couturier et al. *Directional detection of Dark Matter with the MIcro-tpc MAtrix of Chambers*. In *51st Rencontres de Moriond on Cosmology La Thuile, Italy, March 19-26, 2016*, 2016.

[78] B. Gripaios G. F. Giudice and R. Mahbubani. *Counting dark matter particles in LHC events*. *Phys. Rev.*, D85:075019, 2012.

[79] L. Evans and P. Bryant. *LHC Machine. Journal of Instrumentation*, 3(08):S08001, 2008.

[80] S. Lowette. *Accelerator searches for new physics in the context of dark matter*. *J. Phys. Conf. Ser.*, 718(2):022011, 2016.

[81] R. Essig et al. *Working Group Report: New Light Weakly Coupled Particles*. In *Proceedings, Community Summer Study 2013: Snowmass on the Mississippi (CSS2013): Minneapolis, MN, USA, July 29-August 6, 2013*, 2013.

[82] P. C. Schuster J. Alwall and N. Toro. *Simplified models for a first characterization of new physics at the LHC. Phys. Rev. D*, 79:075020, Apr 2009.

[83] D. Alves et al. *Simplified models for LHC new physics searches. Journal of Physics G: Nuclear and Particle Physics*, 39(10):105005, 2012.

[84] J. Abdallah et al. *Simplified Models for Dark Matter Searches at the LHC*. *Phys. Dark Univ.*, 9-10:8–23, 2015.

[85] D. Abercrombie et al. *Dark Matter Benchmark Models for Early LHC Run-2 Searches: Report of the ATLAS/CMS Dark Matter Forum*. 2015.

[86] J. Abdallah et al. *Simplified Models for Dark Matter and Missing Energy Searches at the LHC*. 2014.

[87] G. Aad et al. *The ATLAS Experiment at the CERN Large Hadron Collider*. *JINST*, 3:S08003, 2008.

[88] S. Chatrchyan et al. *The CMS experiment at the CERN LHC*. *JINST*, 3:S08004, 2008.

[89] G. Aad et al. *Search for new phenomena in final states with an energetic jet and large missing transverse momentum in pp collisions at* $\sqrt{s}$ *=8 TeV with the ATLAS detector*. *Eur. Phys. J.*, C75(7):299, 2015. [Erratum: Eur. Phys. J.C75,no.9,408(2015)].

[90] V. Khachatryan et al. *Search for dark matter, extra dimensions, and unparticles in monojet events in proton–proton collisions at* $\sqrt{s} = 8$ *TeV*. *Eur. Phys. J.*, C75(5):235, 2015.

[91] G. Aad et al. *Search for dark matter in events with a hadronically decaying W or Z boson and missing transverse momentum in pp collisions at* $\sqrt{s} = 8$ *TeV with the ATLAS detector*. *Phys. Rev. Lett.*, 112(4):041802, 2014.

[92] CMS Collaboration. *Combination of searches for high-mass resonances in Zgamma final states in proton-proton collisions at sqrts 8 and 13 TeV*. 2016.

[93] G. Aad et al. *Search for new particles in events with one lepton and missing transverse momentum in pp collisions at* $\sqrt{s} = 8$ *TeV with the ATLAS detector*. *JHEP*, 09:037, 2014.

[94] V. Khachatryan et al. *Search for physics beyond the standard model in final states with a lepton and missing transverse energy in proton-proton collisions at* $\sqrt{s} =$ 8 TeV. *Phys. Rev. D*, 91:092005, May 2015.

[95] G. Aad et al. *Search for new phenomena in events with a photon and missing transverse momentum in pp collisions at* $\sqrt{s} = 8$ *TeV with the ATLAS detector*. *Phys. Rev.*, D91(1):012008, 2015. [Erratum: Phys. Rev.D92,no.5,059903(2015)].

[96] V. Khachatryan et al. *Search for new phenomena in monophoton final states in proton-proton collisions at* $\sqrt{s} = 8$ *TeV*. *Phys. Lett.*, B755:102–124, 2016.

[97] D. G. Cerdeno and A. M. Green. *Direct detection of WIMPs*. 2010.

[98] M. W. Goodman and E. Witten. *Detectability of Certain Dark Matter Candidates*. *Phys. Rev.*, D31:3059, 1985.

[99] J. Engel. *Nuclear form-factors for the scattering of weakly interacting massive particles*. *Phys. Lett.*, B264:114–119, 1991.

[100] A. L. Fitzpatrick, W. Haxton, E. Katz, N. Lubbers, and Y. Xu. *The Effective Field Theory of Dark Matter Direct Detection*. *JCAP*, 1302:004, 2013.

[101] N. Anand, A. Liam Fitzpatrick, and W. C. Haxton. *Weakly interacting massive particle-nucleus elastic scattering response*. *Phys. Rev.*, C89(6):065501, 2014.

[102] A. L. Fitzpatrick, W. Haxton, E. Katz, N. Lubbers, and Y. Xu. *Model Independent Direct Detection Analyses*. 2012.

[103] F. J. Kerry and D Lynden-Bell. *Review of galactic constants*. 1986.

[104] T. M. Undagoitia and L. Rauch. *Dark matter direct-detection experiments*. *J. Phys.*, G43(1):013001, 2016.

[105] M. Cirelli, G. Corcella, A. Hektor, G. Hutsi, M. Kadastik, P. Panci, M. Raidal, F. Sala, and A. Strumia. *PPPC 4 DM ID: A Poor Particle Physicist Cookbook for Dark Matter Indirect Detection*. *JCAP*, 1103:051, 2011. [Erratum: JCAP1210,E01(2012)].

[106] M. Pato and F. Iocco. *Mapping dark matter in the Milky Way, a synopsis*. In *Proceedings, 34th International Cosmic Ray Conference (ICRC 2015)*, 2015.

[107] F. Iocco, M. Pato, and G. Bertone. *Evidence for dark matter in the inner Milky Way*. *Nature Phys.*, 11:245–248, 2015.

[108] *Techniques for Nuclear and Particle Physics Experiments*. Springer-Verlang.

[109] J. Billard, L. Strigari, and E. Figueroa-Feliciano. *Implication of neutrino backgrounds on the reach of next generation dark matter direct detection experiments*. *Phys. Rev.*, D89(2):023524, 2014.

[110] L. E. Strigari. *Neutrino Coherent Scattering Rates at Direct Dark Matter Detectors*. *New J. Phys.*, 11:105011, 2009.

[111] E. L. Asamar. *Results from the second CDMSlite run and plans for SuperCDMS SNOLAB*.

[112] J. Cooley. *Background considerations for SuperCDMS*. *AIP Conf. Proc.*, 1549:223–226, 2013.

[113] R. Agnese et al. *Demonstration of Surface Electron Rejection with Interleaved Germanium Detectors for Dark Matter Searches*. *Appl. Phys. Lett.*, 103:164105, 2013.

[114] D. Speller and SuperCDMS Collaboration. *Dark matter direct detection with SuperCDMS Soudan*. *Journal of Physics: Conference Series*, 606(1):012003, 2015.

[115] C. McCabe. *Aspects of DM Phenomenology*. PhD thesis, University of Oxford, 2011.

[116] S. Yellin. *Finding an Upper Limit in the Presence of Unknown Background*. *Physics Review*.

[117] R. Agnese et al. *Search for Low-Mass Weakly Interacting Massive Particles Using Voltage-Assisted Calorimetric Ionization Detection in the SuperCDMS Experiment*. *Phys. Rev. Lett.*, 112(4):041302, 2014.

[118] R. Agnese et al. *Search for Low-Mass Weakly Interacting Massive Particles with SuperCDMS*. *Phys. Rev. Lett.*, 112(24):241302, 2014.

[119] C. E. Aalseth et al. *Results from a Search for Light-Mass Dark Matter with a P-type Point Contact Germanium Detector*. *Phys. Rev. Lett.*, 106:131301, 2011.

[120] R. Agnese et al. *New Results from the Search for Low-Mass Weakly Interacting Massive Particles with the CDMS Low Ionization Threshold Experiment*. *Phys. Rev. Lett.*, 116:071301, Feb 2016.

[121] M. C. Fritts. *Background Characterisation and Discrimination in the Final Analysis of the CDMS II Phase of the Cryogenic Dark Matter Search.* PhD thesis, University of Minnesota, 2011.

[122] S. Agostinelli and others. *Geant4—a simulation toolkit. Nuclear Instruments and Methods in Physics Research Section A: Accelerators, Spectrometers, Detectors and Associated Equipment*, 506(3):250 – 303, 2003.

[123] J. Allison et al. *Geant4 Developments and Applications. IEEE Transactions on Nuclear Science*, 2006.

[124] E. L. Asamar. *Measurement of the radioactivity levels in SuperCDMS Soudan using the gamma-ray spectrum.* Private webpage, SuperCDMS collaboration.

[125] P. K. Sinervo. *Definition and Treatment of Systematic Uncertainties in High Energy Physics and Astrophysics.*